Diplomarbeit

Surface Plasmon Polaritons in Graphene

durchgeführt von

Simone Schuler
0725285/439

am
Institut für Photonik
der Technischen Universität Wien

unter der Leitung von
Ass.Prof. Dipl.-Ing. Dr.techn. Thomas Müller
und
Univ.Prof. Mag.rer.nat. Dr.rer.nat. Karl Unterrainer

Contents

1 Graphene **1**
- 1.1 Electronic properties of graphene . . . 2
- 1.2 Optical properties of graphene . . . 5
- 1.3 Synthesis of graphene . . . 8
  - 1.3.1 Micromechanical cleavage . . . 8
  - 1.3.2 Chemical vapor deposition . . . 8
  - 1.3.3 Other techniques . . . 11
- 1.4 Characterization of graphene . . . 12
  - 1.4.1 Optical microscopy . . . 12
  - 1.4.2 Raman spectroscopy . . . 13
  - 1.4.3 Fourier spectroscopy . . . 16
  - 1.4.4 Mobility measurements . . . 18

2 Plasmonics **21**
- 2.1 The Plasma model . . . 21
  - 2.1.1 Dispersion relation of the free electron gas . . . 23
- 2.2 Surface plasmon polaritons . . . 23
  - 2.2.1 TE and TM surface waves . . . 24
  - 2.2.2 Surface plasmon polaritons . . . 25
  - 2.2.3 Excitation of plasmons at planar interfaces . . . 29
- 2.3 Plasmons in graphene . . . 33
  - 2.3.1 Dispersion relation of graphene . . . 34

3 Experimental **37**
- 3.1 Processing techniques . . . 37
  - 3.1.1 Electron beam lithography . . . 37
  - 3.1.2 Reactive ion etching . . . 39
  - 3.1.3 Optical lithography . . . 39
  - 3.1.4 Metalization . . . 40
- 3.2 Sample preparation . . . 41
  - 3.2.1 Graphene patterning . . . 42
  - 3.2.2 Aperture fabrication . . . 43
  - 3.2.3 Doping of graphene . . . 44

3.3 Characterization with Raman spectroscopy 45
3.4 Transmittance measurements 47

4 Conclusion and Outlook **53**

Abstract

Collective oscillations of electrons are referred to as plasmons. Graphene, the two dimensional form of carbon, has very interesting properties promoting plasmons, such as tunable bandgap, long photon life time and strong confinement. This work deals with surface plasmon polaritons in graphene in the mid infrared. Graphene gratings based on CVD graphene were fabricated using electron beam lithography and reactive ion etching. Two gratings, with grating periods of 250 nm and 440 nm, respectively, and 50 % fill factor were fabricated to study the influence of the grating period on the resonance behavior. The gratings were characterized at room temperature using Raman and Fourier spectroscopy. Three dominant resonance peaks were observed. Two of these resonance peaks arise from interactions of the graphene with surface phonon modes of the silicon dioxide substrate. The third peak is referred to the surface plasmon polariton in the patterned graphene. Comparison of the resonance spectra of the two gratings brings out three major aspects. The position of all resonance peaks shifts to higher frequencies when the grating period is increased. The third resonance peak becomes narrower with increased grating period. Furthermore, a change of the grating period has an influence on the spectral weight of the phonon modes. Increasing the grating period leads to a transfer of the the spectral weight from the second to the first phonon mode.

Kurzfassung

Als Plasmonen werden Oszillationen der Elektronendichte in Metallen bezeichnet. Die Plasmonenresonanz wird durch die Geometrie festgelegt. Graphen, die zweidimensionale Form von Kohlenstoff, zeichnet sich durch seine außergewöhnlichen Eigenschaften aus. Dazu gehört eine durchstimmbare Bandlücke, eine lange Lebensdauer und eine ausgeprägte Lichtführung. Diese Eigenschaften lassen sich für die Ausbreitung von Plasmonen nutzen. In dieser Arbeit werden Oberflächenplasmonen in Graphen im mittleren Infrarot Bereich untersucht. Oberflächenplasmonen bezeichnen evaneszente Wellen, die sich parallel zu einer Grenzschicht ausbreiten. Zur Anregung der Plasmonenschwingung wurden Gitterstrukturen mittels Elektronenstrahllithographie und einem reaktiven Ionenätzverfahren aus Graphen gefertigt. Zwei Gitterstrukturen mit einer Gitterperiode von 250 nm und 440 nm und einem Füllfaktor von 50 % wurden hergestellt, um den Einfluss der Gitterperiode auf die Plasmonenresonanz zu untersuchen. Zur Charakterisierung der Gitterstrukturen wurden Ramanmessungen sowie Fouriermessungen durchgeführt. Drei dominante Resonanzen konnten bei polarisationsabhängigen Messungen mit dem Fourierspektrometer beobachtet werden. Zwei davon treten auf Grund von Wechselwirkungen mit Phononen des Silizium Subtrates auf. Die dritte Resonanz lässt auf die Anwesenheit von Oberflächenplasmonen schließen. Ein Vergleich der Resonanzspektren beider Gitter zeigt, dass eine Erhöhung der Gitterperiode hat eine Verschiebung aller Resonanzen zu höheren Frequenzen zur Folge. Weiters wird die charakteristische Resonanzüberhöhung des Plasmons schmaler und stärker ausgeprägt. Die beiden Resonanzüberhöhungen auf Grund der Wechselwirkung mit dem Substrat ändern sich in ihrem spektralen Gewicht. Durch eine Erhöhung der Gitterperiode verstärkt sich die Absorption der ersten Resonanz, während die zweite Resonanz abgeschwächt wird.

Introduction

Carbon plays a unique role in nature. Carbon occurs in many forms such as diamond (3D), graphite (3D), nanontubes (1D) or fullerenes (0D). The latter were found 10 - 20 years ago. 2004 Andre Geim and Konstantin Novoselov from the University of Manchester found the two dimensional form which was believed to be unstable. This two dimensional from of carbon is referred to as graphene and is one of the most popular research topics in physics today. Properties, such as high electron mobility, high thermal conductivity, broadband absorption, and many others allows graphene to support applications in many different areas. Sensing applications, broadband modulators, touch sensitive displays are only a few. Graphene allows down-scaling and is thus ideal for nano-scaled electronics. Furthermore, it makes the integration of electronics and optical components on silicon possible. The unique properties of graphene in terms of conductivity and the tunability of the Fermi level by electrical or chemical doping as well as the broad absorption make graphene also an ideal candidate for novel plasmonic devices. Plasmons play a fundamental role in the dynamic response of light matter interactions. Plasmons have the ability to confine light in small dimensions beneath the diffraction limit, enabling various applications. Commonly plasmonic structures are realized with metals, such as gold or silver. Devices based on this materials suffer from large losses, and thus from a small photon life time. Using graphene instead of noble metals, one can benefit from its excellent electrical and optical properties. The strong confinement, the tunability by electrical gating or chemical doping, as well as low losses and long lifetime make graphene plasmonics an interesting topic. Ju et. al [1] demonstrated graphene plasmonics for tunable terahertz metamaterials and Yan et. al [2] depicted the properties of graphene plasmonics in the mid infrared range. Light manipulation with graphene offers new ways towards optoelectronics, as it can be easily integrated on silicon.

This work deals with plasmonic structures made out of graphene in the mid infrared range. Chapter 1 gives an overview on the electronic and optical properties of graphene. Synthesis and characterization techniques are resumed in this chapter. Chapter 2 introduces plasmons with the focus on surface plasmons due to the two dimensional form of graphene. Furthermore, the excitation of plasmons is contained in this chapter. The experimental work is summarized in chapter 3, including fabrication techniques and results.

Chapter 1

Graphene

In 2004 Andre Geim and Konstantin Novoselov extracted a monolayer of graphene from graphite and revealed that graphene can be detected with an optical microscope when it is placed on an ordinary silicon dioxide substrate. With their research they opened the door to novel two dimensional materials and were therefore awarded with the Nobel Prize in Physics 2010 "for groundbreaking experiments regarding the two-dimensional material graphene".

In 1947 the first bibliographical reference was given by P.R. Wallace, who illustrated the nearest neighbor tight binding model for the band structure of a single layer of graphene. Graphene builds the basis of all carbon allotropes. In 1985 Robert F. Curl Jr., Sir Harold W. Kroto, and Richard E. Smalley found the zero dimensional form of carbon, fullerenes or buckyballs. They obtained molecules of 60 carbon atoms arranged in a spherical form by vaporizing graphite rods with a laser in helium gas atmosphere. Another form of low dimensional carbon is a cylindrical arrangement of carbon atoms, referred to as carbon nanotubes. This is the one dimensional form and was found by Sumio Iijima in 1991. Until now several techniques have been found to produce nanotubes, such as laser ablation or chemical vapor deposition and many others. A couple of years have past away until researchers found the two dimensional form graphene. The planar form of graphene first has been assumed not to be stable with respect to the formation of nanotubes or buckyballs.

Since 2004 graphene has attracted a lot of attention in research. Its excellent properties enable the use of graphene in a wide range of electronic and optical applications. The anomalous Quantum Hall effect, the tunable bandgap, the high elasticity and mechanical stability and the low absorption of graphene, enhanced the interest in this field of research.

This chapter concerns the atomic structure of graphene and the resulting electronic and optical properties. Furthermore, an overview of synthesis techniques and characterization methods is given.

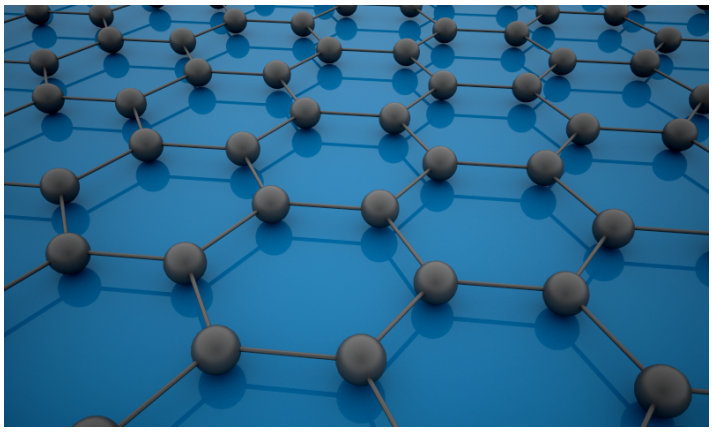

Figure 1.1: Sketch of graphene on a substrate.

1.1 Electronic properties of graphene

The electronic properties of graphene are the result of its atomic structure. The fundamental building block of graphene is the carbon atom. A carbon atom has 6 electrons, where 2 electrons are located in the $1s$ orbital and are strongly bonded with the core. The other 4 electrons occupy the $2s$ and the $2p$ orbitals. The $2p$ orbitals are very directional, each $2p$ orbital has two phased lobes which are opposite to each other but lie on one axis. The orbitals are shown in figure 1.2 on the left side.

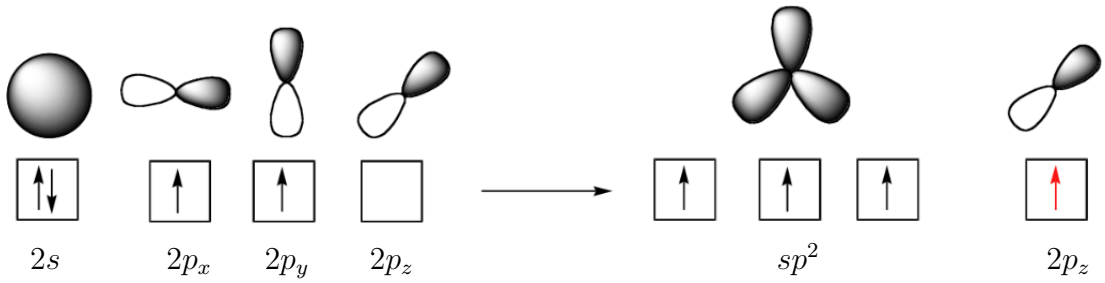

Figure 1.2: Orbitals of a carbon atom. The spherical $2s$ orbitals and the phased lobes of the directed $2p$ orbital is shown on the left side. The right side depicts the sp^2 hybrid orbitals and the remaining p_z orbital. Due to two valid electrons from the $2s$ orbital, hybridization can only occur in two dimensions. Taken from [3].

The $2s$ orbital provides two electrons, thus it can link only with two of the three $2p$ orbitals. This link is referred to as hybridization of the orbitals. The hybrid orbitals are responsible for the hexagonal form of graphene. Graphene is based on carbon atoms which has three sp^2 orbitals which are build from the $2s$ and two $2p$ orbitals. The hybrid orbitals are shown in figure 1.2 on the right side.

Because the two $2p$ orbitals lie in plane, the three sp^2 hybrid orbitals also lie in the same plane. Since more than one atom is involved, they interact with each other. When two or more atomic orbitals overlap, the orbitals smear out and bonds are formed. The first covalent bond which is formed between two atoms is the sigma (σ) bond. The sp^2 orbitals share the electron density along the bonding axis which results in a more stable arrangement then before. The potential energy is in this case lowered by the bond energy. The new sigma molecular orbital formed by the orbitals from the interacting atom can be written as $\sigma = 1sp_1^2 + 1sp_2^2$. A second, also created molecular orbital $\sigma^* = 1sp_1^2 - 1sp_2^2$, is referred to as anti-bonding molecular orbital. The σ bonding molecular orbital describes the shared electron density between two bonding atoms along the bond axis. This orbital is usually occupied with electrons. In contrast the σ^* orbital is usually empty. The covalent σ and σ^* bond causes the hexagonal lattice structure of graphene. Beside the sp^2 orbitals, the remaining p_z orbitals are able to form bonds if they overlap. The so-called π bonds generate the a molecular orbital $\pi = p_{z,1} + p_{z,2}$ and the anti-bonding orbital $\pi^* = p_{z,1} - p_{z,2}$. The electrons in this state are weakly bonded and therefore responsible for the electronic transport properties.

Lattice structure

In graphene, carbon atoms are arranged in a hexagonal structure, as illustrated in figure 1.3. The carbon atom has a distance of $a = 1.42$Å to its next neighbor. Each carbon atom shares a σ bond with one of it's neighbors. The π and π^* orbitals are responsible for most of the electronic properties in graphene.

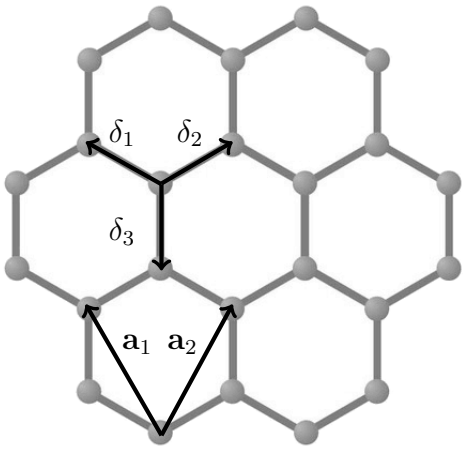

Figure 1.3: Graphene has a hexagonal lattice structure. One unit cell contains two carbon atoms. The distance between the two atoms is $a = 1.42$ Å.

The lattice can be described with the lattice vectors

$$\mathbf{a}_1 = \frac{a}{2}(3, \sqrt{3}), \tag{1.1a}$$

$$\mathbf{a}_2 = \frac{a}{2}(3, -\sqrt{3}), \tag{1.1b}$$

which gives the distance to the next atoms A and B. The vectors from an atom A to its neighboring atoms are given by

$$\delta_1 = \frac{a}{2}(1, \sqrt{3}), \tag{1.2a}$$

$$\delta_2 = \frac{a}{2}(1, -\sqrt{3}), \tag{1.2b}$$

$$\delta_3 = a(1, 0). \tag{1.2c}$$

These vectors are used in the tight-binding approximation to derive the band structure of graphene, where electrons can hop to nearest neighbor atoms ($\delta_{1,2,3}$) or next nearest neighbor atoms ($\mathbf{a}_{1,2}$). The band structure was derived by P.R. Wallace in 1947 as

$$E_{\pm}(\mathbf{k}) = \pm t\sqrt{3 + f(\mathbf{k})} - t' f(\mathbf{k}), \tag{1.3}$$

with

$$f(\mathbf{k}) = 2\cos\left(\sqrt{3}k_y a\right) + 4\cos\left(\frac{\sqrt{3}}{2}k_y a\right)\cos\left(\frac{3}{2}k_x a\right), \tag{1.4}$$

where $t(\approx 2.7\,\mathrm{eV})$ describes the nearest-neighbor hopping energy and $t'(0.02t \leq t' \leq 0.2t)$ [4] describes the next nearest neighbor hopping. The plus sign corresponds to the upper π band and the minus to the lower π band.

The valence band formed by the π bonds and the conduction band formed by the π^* bonds touch at 6 points, the so called Dirac points. There are two sets of Dirac points K and K' which can be distinguished, due to symmetry. The Dirac points are the transition between valence and conduction band. Near these Dirac points K and K' the electron energy is linearly dependent on the wave vector $\mathbf{k}$. The band structure in this regime is given by two cones touching at the Dirac points, due to non-existing interactions between the bonding π and anti bonding π^* orbitals [5]. The linear dispersion relation near the Dirac points can be described with the Dirac equation for mass less Fermions [6]. The charge carriers around the K points have zero mass. Applying a Taylor expansion around $\mathbf{K}$ or $\mathbf{K}'$ results in

$$E_{\pm}(\kappa) \approx \pm\hbar v_F \mid \kappa \mid, \tag{1.5}$$

where $\kappa = \mathbf{k} - \mathbf{K}$ and v_F is the Fermi velocity, given by $v_F = 3ta/2 = 1 \times 10^6\mathrm{m/s}$. The equivalent band structure for electrons and holes and the zero bandgap induce an equal behavior for both charge carriers. The spectrum around the Dirac point, illustrated in figure 1.4, is similar to the spectrum of mass less Dirac Fermions. This is due to the fact that the unit cell consists of two atoms, where interaction between the electrons are possible, leading to the formation of energy bands [7].

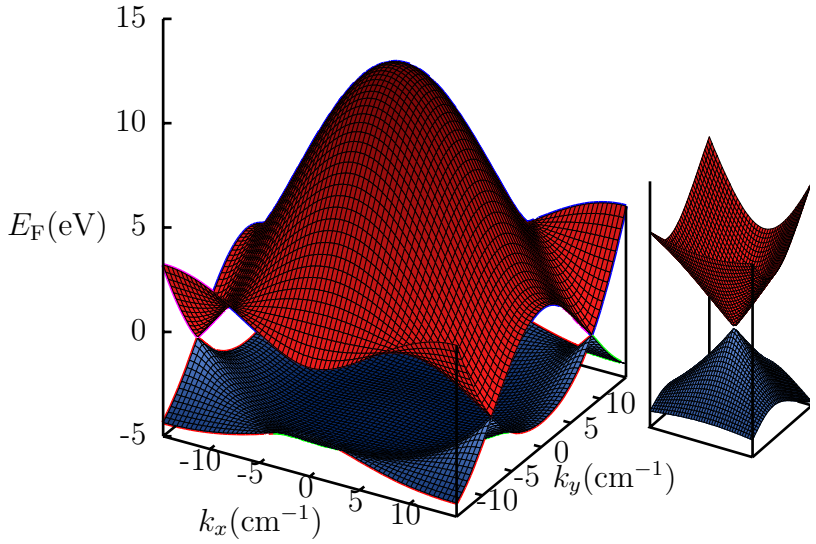

Figure 1.4: Band structure of graphene, calculated with nearest($t = 2.7\,\mathrm{eV}$) and next nearest($t' = 0.2t\,\mathrm{eV}$) neighbor hopping. If $t' = 0$ both bands are symmetric, electron and holes behave similar. Around the crossing points, the so called Dirac points, the electron energy depends linearly on the wave vector.

1.2 Optical properties of graphene

Graphene has unique optical properties, in comparison to other materials. Although graphene is only a single atom layer thick it can be visualized. The independence of the transmittance over a wide spectral range as well as the linear dispersion relation make graphene an ideal material for optical and optoelectronic applications. For vertical (k-conserving) transitions, the light transmission through free standing graphene can be derived by Fresnel's law for thin films by

$$T = \left(1 + \pi\frac{\alpha}{2}\right)^{-2} \cong 1 - \pi\alpha \approx 0.977, \tag{1.6}$$

where $\alpha = e^2/4\pi\epsilon_0\hbar c$ denotes the fine structure constant. The assumption holds in a wide spectral range from the visible to the mid infrared. In the far infrared the absorption is governed by intraband absorption. Whereas the spectral range from the mid infrared to the ultraviolet are dominated by interband transitions [5].

Intraband absorption

Intraband absorption, also referred to as free carrier absorption, is the dominant process in the infrared between 1 µm and 15 µm. Momentum conservation is fulfilled due to an indirect transition of a photon and a phonon as illustrated in figure 1.5 (left). The intraband absorption can be described by the Drude model [8]

$$\sigma_D(\omega) = \sigma_0 \frac{4E_\mathrm{F}}{\pi} \frac{1}{\hbar\frac{1}{\tau} - \imath\hbar\omega}, \tag{1.7}$$

with $\sigma_0 = \dfrac{\pi e^2}{2h}$ and τ denoting the average electron scattering time. In figure 1.5 (right) the optical Drude conductivity σ_D is plotted assuming a Fermi level $E_F = 200\mathrm{meV}$ and an electron scattering rate $\tau = 50\mathrm{fs}$.

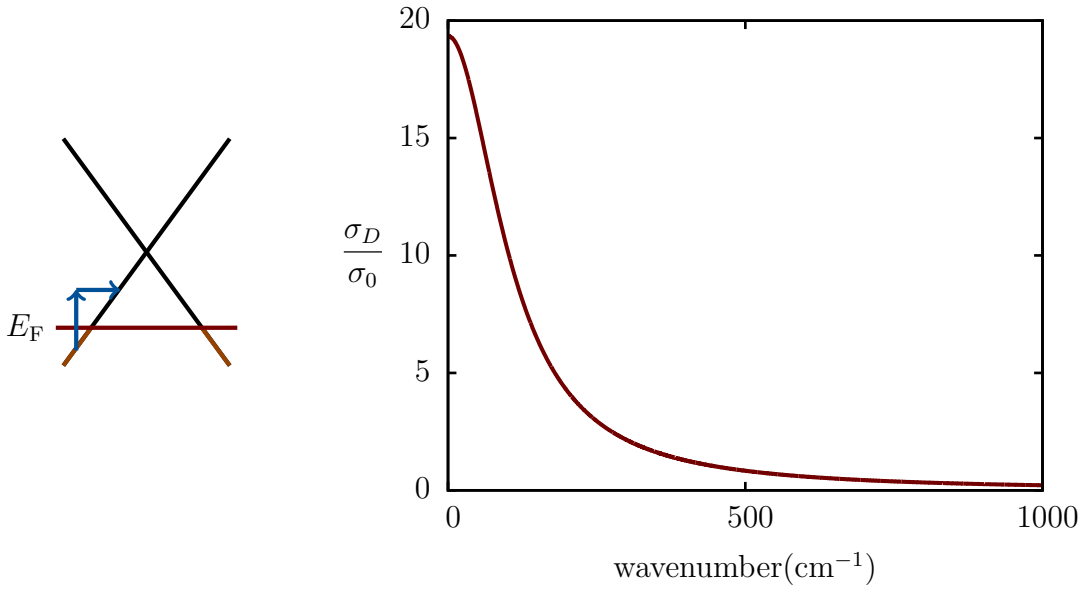

Figure 1.5: Illustration of the free carrier absorption or intraband absorption in graphene (left). To conserve the momentum a scattering process with phonons is needed. The right part of the figure shows the absorption of graphene in the far infrared range, due to free carrier absorption. The Fermi level is taken $E_\mathrm{F} = 200\mathrm{meV}$ and the electron scattering time is taken as $\tau = 50\mathrm{fs}$.

Interband absorption

For frequencies beyond the far infrared, light absorption in graphene is dominated by interband optical transitions. The absorption arises from direct optical

transitions between the valence and conduction bands as illustrated in figure 1.6. According to Ref.[9], the optical conductivity near the Fermi level results in

$$\sigma_{inter}(\omega, T) = \frac{\pi e^2}{4h}\left[\tanh\left(\frac{\hbar\omega + 2E_F}{4k_{\mathrm{B}}T}\right) + \tanh\left(\frac{\hbar\omega - 2E_{\mathrm{F}}}{4k_{\mathrm{B}}T}\right)\right], \tag{1.8}$$

depending on the Fermi level E_F and the temperature T. Due to Pauli blocking transitions beneath $2\cdot \mid E_{\mathrm{F}} \mid$ are not allowed.

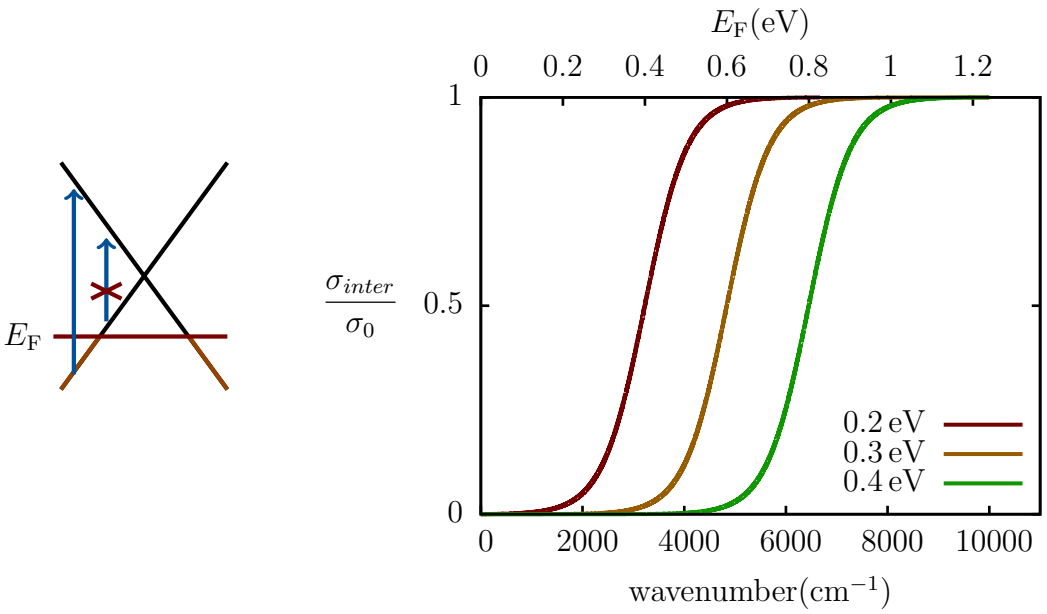

Figure 1.6: Illustration of the interband absorption in graphene (left). Due to Pauli blocking photons with an energy smaller than $2 \mid E_{\mathrm{F}} \mid$ are not absorbed. The right part of figure shows the interband absorption calculated with equation 1.8, plotted at room temperature for different Fermi levels.

As a result, controlling the Fermi level via doping or electrostatic gating allows controlling of the interband transitions. In graphene the Fermi level can be shifted over a range of hundreds of cm^{-1} through electrostatic gating. This wide tunability is due to graphene's linear dispersion and its low density of states. It allows to a widely tunable optical response, where energies below $2\cdot|E_{\mathrm{F}}|$ are suppressed and energies above $2\cdot|E_{\mathrm{F}}|$ unaffected [8]. Figure 1.6 shows the absorption shift, induced by a change of the Fermi level. The interband transition shifts with higher Fermi level to higher frequencies. Assuming zero temperature and undoped graphene, equation 1.8 reduces to

$$\sigma_0 = \frac{\pi e^2}{2h}. \tag{1.9}$$

The optical sheet conductivity σ_0 can be extracted from the tight binding model [10]. By measuring the interband absorption, it is possible to evaluate the doping concentration of graphene. The relation between the Fermi level E_{F} and the charge

carrier density n is given as

$$E_{\mathrm{F}} = \hbar v_{\mathrm{F}} \sqrt{\pi n}, \tag{1.10}$$

where $v_{\mathrm{F}} = 1.1 \times 10^6\,\mathrm{m/s}$ denotes the Fermi velocity.

1.3 Synthesis of graphene

In 2004 Novoselov et al. has demonstrated the repeatable fabrication of graphene through micro mechanical cleavage. This technique was used to produce graphene flakes with a size of a few µm. Micro mechanical cleaved graphene has the best quality in terms of defects, mobility and optoelectronic properties. However, to cover applications like flat panel displays, photo voltaic cells as transparent electrodes or integrated electronics, graphene has to be produced on a larger scale. Therefore synthesis techniques like chemical vapor deposition (CVD) [11] or techniques based on SiC [12] are required. Wafer-scale graphene can be grown by chemical vapor deposition(CVD) from carbon-containing gases on catalytic metal surfaces or by surface segregation on carbon dissolved in the bulk of such metals [13]. Another way to produce graphene, is the chemical reduction from graphite oxide [14] or high temperature annealing of silicon carbide (SiC) [12].

This section gives an overview of different techniques to synthesize graphene.

1.3.1 Micromechanical cleavage

Graphite is based on stacks of graphene which are held together by van der Waals forces. Thus, it is possible to prepare a individual monolayer of graphene by so called micromechanical cleavage [10]. Starting from graphite, which is deposited between an adhesive tape and repeatedly peeled away, stacks become separated. Subsequently, the tape with the thinned graphite is then placed and pressed on against a substrate. Due to Van der Waals forces, some of the graphene monolayers remain on the substrate after removing the adhesive tape. Graphene monolayer flakes of a few µm in size may be produced with this procedure. The shape of these exfoliated flakes is very irregular and their orientation cannot be controlled [13]. However, graphene fabricated with micromechanical cleavage is of the highest available quality. The technique is also used to fabricate two dimensional layers from various other materials, such as MoS2, BN.

1.3.2 Chemical vapor deposition

Chemical vapor deposition is the most common way to produce graphene on large scale. Thin films are deposited on a substrate from a vapor phase by chemical reactions. Figure 1.8 illustrates the principle procedure. Carrier gases are led into the chamber which diffuse to the hot surface and become absorbed. To start the reaction, the surface has to be heat up to provide sufficient energy to thermally

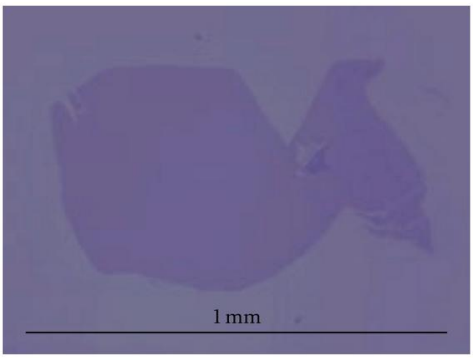

Figure 1.7: One of the biggest monolayer of graphene fabricated by micromechanical cleavage on silicon dioxide. Taken from [15].

crack the adsorbed gas molecules. The nonvolatile fragments remain at the surface while the volatile fragments desorb, diffuse and become dispatched.

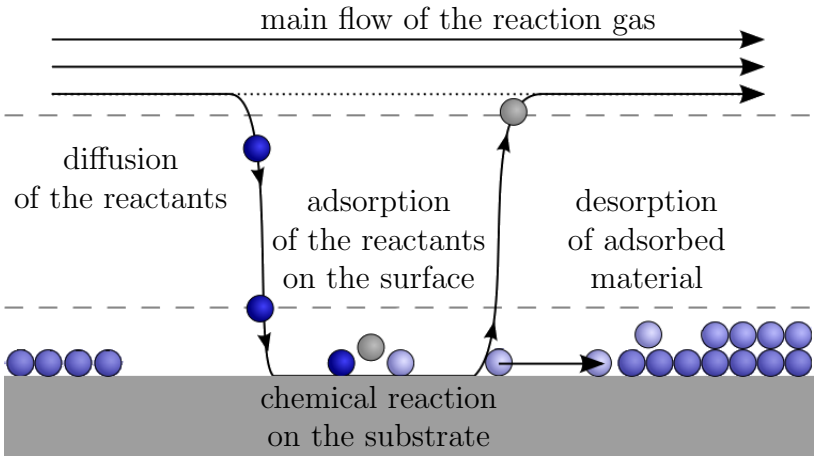

Figure 1.8: The principle of chemical vapor deposition is the controlled decomposition of carrier gas on hot surfaces. The gas molecules are approximated with a controlled gas flow and thermally cracked on the surface. Nonvolatile molecules remain on the surface while the other molecules are transported away through the gas flow.

Important parameters to control the CVD process are the gas flow, the energy and the chamber pressure. The energy can be delivered thermally, by heating the substrate or electrically via a HF-plasma and is responsible for the reaction. The chamber pressure is important for the transport to and from the reactive surface. For graphene growth a metal is needed as a catalyst. The function of these catalysts is to lower the energy barrier of the reaction [16]. Different metals, such as Cu[11], Ni[17], Pt[18] or Ir[19] are commonly used as carrier substrate for

graphene growth. During the CVD process a precursor gas which contains C, for example C_2H_2 or CH_4, is fed into the chamber. The molecules in the precursor gas crack at the surface and the carbon atoms remain at the surface in areas with lower energy such as grain boundaries or defects, where the graphene starts to grow. The H_2 diffuses back and gets dispatched. Due to the fact that metals are non monochrystalline, graphene builds islands arround the grain boundaries. Figure 1.9 depicts a single layer of graphene grown on a copper foil.

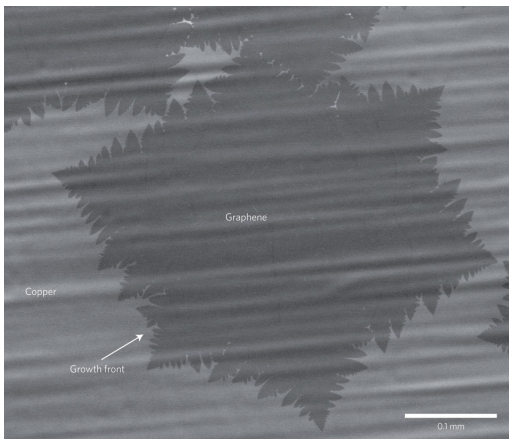

Figure 1.9: Scanning electron microscopy image of a large graphene flake (single crystal) grown on copper by chemical vapor deposition. Taken from [20].

Chemical vapor deposition of graphene has the advantage of low cost and scalable production. A disadvantage is that the growth takes place on a metal but most of the applications are build on an insulator. Furthermore, graphene grown with chemical vapor deposition has a lower quality and thus lower mobility compared to micromechanically cleaved graphene. Mobilities of about $2000 - 4000\,\mathrm{cm^2V^{-1}s^{-1}}$ have been observed in graphene grown on a metal [21], whereas for micromechanically cleaved graphene mobilities of around $10^6\,\mathrm{cm^2V^{-1}s^{-1}}$ have been observed [22].

CVD graphene growth on Nickel

Nickel is a common catalyst for the growth of graphene by chemical vapor deposition. The Ni surface gets annealed around 800°C [23] which leads to grain growth. Methane CH_4 is varnished into the reaction chamber to start the deposition process. During the deposition the CH_4 molecules crack at the surface. The carbon atoms diffuse into the Ni while the rest of the fragments become depatched. Before taking the sample out, the reaction chamber is cooled down, so that the dissolved carbon atoms adsorb on the surface. Raina et al. [17] present in their work monolayer regions with a size up to 20µm and regions consisting between 1 to 12 layers of graphene. De Arco et al. [23] have reported domain sizes of $1 - 2$µm which is due to the grain size of the Ni film. Because of considerable solubility of

C in Ni a control of the number of layers is difficult. The process mainly depends on the solubility of carbon atoms into the nickel.

CVD graphene growth on Copper

Beside Nickel also Copper is a very common catalyst for graphene growth. Because of the negligible solubility of carbon atoms in Cu around 1000°C, the graphene growth takes only place on the surface. Large area graphene with more than 95% monolayer were grown on copper foils by chemical vapor deposition with methane CH_4. If the Cu surface is completely covered with graphene, the growth process is terminates by itself.

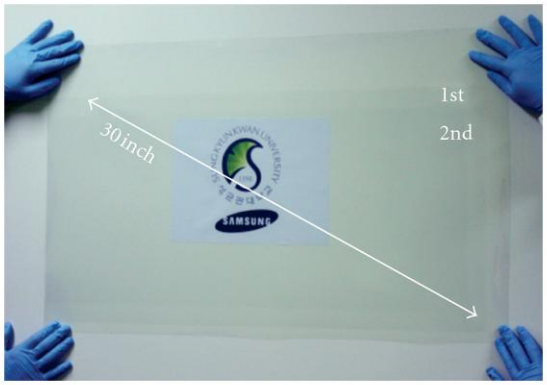

Figure 1.10: Graphene sheet, grown on copper with chemical vapor deposition. To transfer the sheet, is was coated with polyethylene terephthalate (PET). Taken from[24].

Transfer of graphene

Since most applications of graphene are build on insulators, graphene grown on metal has to be transferred to the target substrates. A common way is to cover the graphene sheet with Polymethylmethacrylate (PMMA). The metal is removed by wet chemical etching. After wet chemical etching the graphene sheet floats on the etchant. The graphene is scooped out followed by a drying process.

1.3.3 Other techniques

Silicon Carbide

Emtsev et al. [12] have demonstrated the growth of graphene on insulating silicon carbide by annealing the substrate in vacuum. They started with an etching process where the semi-insulating $6H - SiC$ substrates were etched with hydrogen.

After cooling and heating the substrate surface damages are removed. Parallel traces of graphene with a width up to 3µm and a length of 50µm were produced with this process.

Molecular beam deposition

Graphene can be deposited onto a nickel substrate by using molecular beam deposition technique. Ethylene (C_2H_2) is thermally cracked at 1200°C and deposited onto the Nickel. The substrate was heated up to 800°C to form a high quality graphene monolayer. This was demonstrated by Zhan et al. [25].

Chemical synthesis

Another possibility is liquid phase exfoliation, where graphite powder is suspended in a solvent by ultrasonication. Up to 70% single layer graphene can be achieved by sonication in water and sodium deoxycholate followed by sedimentation [22].

1.4 Characterization of graphene

Even though micromechanical cleavage is a straight forward way to produce graphene, it is difficult to find monolayer crystals on a substrate. Visualization techniques to find and characterize graphene are optical microscopy [26] and Raman spectroscopy. Raman spectroscopy [27] also provides information about the number of layers, defects and impurities. Beside these techniques atomic-force, scanning-tunneling and electron microscopy are common techniques to detect and characterize graphene. The bandstructure as well as mobility measurements give information about the number of layer and defects. The latter technique requires electric contacts.

1.4.1 Optical microscopy

As mentioned before, using optical microscopy, it is straight forward, to find graphene on a substrate. Graphene absorbs only 2.3 %, thus it is important to achieve a good contrast, that graphene becomes visible. Beside the substrate, the light source affects the contrast. Blake and Hill demonstrated that the contrast depends mainly on the thickness of the silicon dioxide and the wavelength of the light source. They used a model based on Fresnel's law to figure out the influence of these two parameters. High contrast appears, using a silicon substrate with 300nm silicon dioxide and a green light source ($\lambda = 560$nm). Using blue light or a substrate with 200nm silicon dioxide makes the graphene invisible. Even better contrast can be achieved when green light is used and the graphene is deposited

onto substrates with 90nm SiO_2. Blake and Hill also demonstrated that it is possible to estimate the number of layers by the change of the optical contrast for $1, 2$ and 3 layers [26].

1.4.2 Raman spectroscopy

When atoms or molecules are exposed with monochromatic light, the photons scatter. Most photons experience elastic scattering and retain their energy. A small part of the photons experience an inelastic scattering process. After the scattering process these photons have a different energy. This effect was observed by C.V. Raman, who was honored for his work with the Nobel Price in Physics in 1930 [28].

The shifted spectral lines are referred to as Raman lines. This lines occur from an inelastic scattering process between the molecule and the excitation photons. The interaction with the light causes scattering of the incoming light at atoms, molecules or crystals. Three kinds of scattered light can be observed as illustrated in figure 1.11.

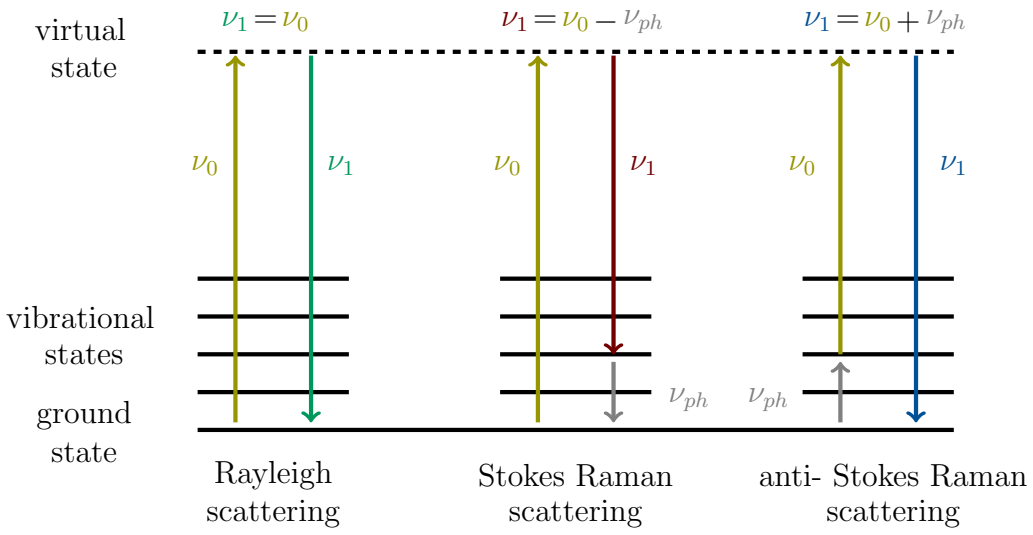

Figure 1.11: Illustration of the Rayleigh and the Raman effect. The Rayleigh process is an elastic process. The scattered light retains the excitation frequency. The Raman process describes an inelastic scattering process between atoms or molecules and photons. One can distinguish between two different processes. Due to emission of a phonon $\nu_1 = \nu_0 - \nu_{ph}$ the photon loses energy by excitation of a vibrational mode. This is referred to as Stokes Raman scattering. The second process, referred to as anti-Stokes Raman process is due to the absorption of a phonon $\nu_1 = \nu_0 + \nu_{ph}$. The photon acquires energy by de-excitation of a vibrational mode.

An elastic collision between an atom or molecule and a photon does not affect the energy state of the molecule. The wavelength of the detected light ν_1 retains the excitation wavelength ν_0. This process is referred to as Rayleigh process and illustrated in figure 1.11 (left). An inelastic scattering process leads to a change of the detected wavelength. The molecule is excited in an excited vibrational state. Resulting in a lower frequency $\nu_1 = \nu_0 - \nu_{ph}$ of the detected light in comparison to the excitation light. This effect is illustrated in the middle part of figure 1.11 and referred to as Stokes Raman scattering. Another possibility is an inelastic scattering process, where the molecule occupies a lower energy state as before, where the frequency of the detected light is $\nu_1 = \nu_0 + \nu_{ph}$. The so-called anti-Stokes Raman scattering process is only possible if the exposed molecule is located in an excited state.

The frequency change of the anti-Stokes Raman scattering is due to rotational and vibrational transitions of the molecules [28]. The energy which is delivered to or from a photon, is equivalent to the energy between two energy niveaus of the molecule. Raman spectroscopy is a non-contact, reflective technique and can be performed under ambient conditions.

A typical Raman spectrometer consists of a monochromatic light source, a microscope which gathers the light and a grating spectrometer. Figure 1.12 depicts the setup of a Raman spectroscopy system. The monochromatic light from the laser source is restricted by a pinhole, deflected by a wavelength selective dichroic mirror and focused on the sample surface with an objective lens. The same lens gathers the scattered light from the sample. The back scattered light passes through the dichroic mirror. The pinhole in front of the fiber coupler allows only light from the focal plane to pass through, resulting in a high resolution. The light is then transported trough an optical fiber to the spectrometer. In the spectrometer the light is split by gratings or prisms into the different wavelengths and read out by a CCD detector. Due to the weak signal originating from the Raman scattering, sensitive CCD detectors are required.

Raman spectroscopy of graphene

As the properties of single and multilayer graphene differ dramatically, it is important to determine the number of layers. A reliable possibility to identify the number of layers is Raman spectroscopy. Furthermore, the defect and impurity densities can be measured by Raman spectroscopy. There are two typical peaks in the Raman spectra of graphene and other graphitic materials [6], the so-called G band which is located at around $1580\,\mathrm{cm}^{-1}$ and the 2D peak which is located at around $2700\,\mathrm{cm}^{-1}$, as illustrated in figure 1.13 for graphene (red) and graphite (blue). Defects and impurities are typically indicated by the D band around $1350\,\mathrm{cm}^{-1}$. In-plane vibrations of the sp^2 carbon atoms are responsible for

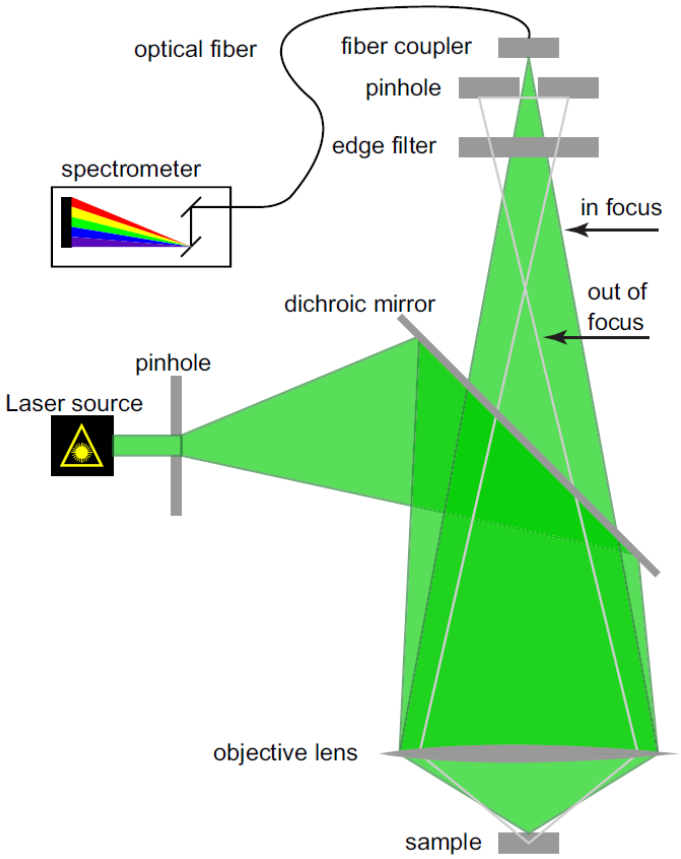

Figure 1.12: Sketch of a Raman spectrometer. The monochromatic light is deflected using a wavelength selective dichroic mirror and is focused on the sample surface via an objective lens. The scattered light is gathered and transferred through an optical fiber to a grating spectrometer. The pinhole in front of the fiber coupler limits the angular distribution, thus only light with the right focal length (green) can pass through. Taken from [29].

the G band. This line is most prominent because it is a characteristic peak in the spectra of graphitic materials. The position of the the G band is very sensitive to the number of layers. Hence, determination of the number of layers is possible. The 2D band, historically referred to as the G′ band, arises from a two phonon resonance process, involving phonons near the **K** point [6]. The 2D band can also be used to determine the layers. With increasing layer number both the position and the shape changes. The Lorentzian 2D peak broadens, the symmetry does not hold any longer and the peak shifts. Another adequate method to determine the layer number, is the relation between the intensity of the 2D- and the G-band. High quality monolayer graphene has a ratio of around two. The D band is induced by defects of the lattice structure of graphene, such as edges.

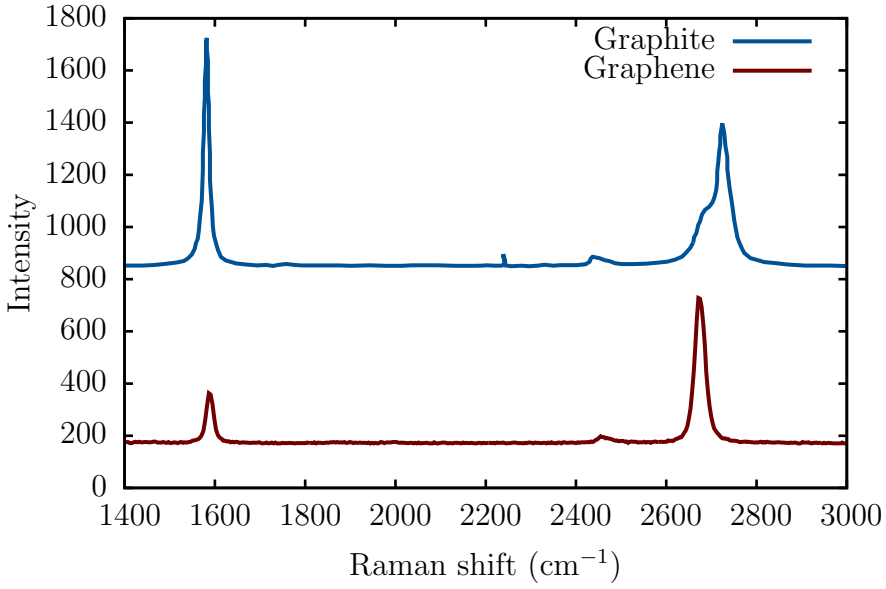

Figure 1.13: Raman spectra of a monolayer graphene (red) and graphite (blue), showing the characteristic G band located at $\sim 1580\,\mathrm{cm}^{-1}$ and the 2D band located at $\sim 2700\,\mathrm{cm}^{-1}$[27]. The G band results from in-plane vibrations of the sp^2 carbon atoms. The 2D band arises from a two phonon process.

1.4.3 Fourier spectroscopy

Fourier spectroscopy is a technique to examine the light matter interaction over a large spectral range. Typically absorption or emission is measured. The technique is based on the measurement of the coherence of electromagnetic radiation. As the name Fourier spectroscopy reveals, the Fourier transformation plays an important role to evaluate the measured data. Characterizing graphene, Fourier transform infrared spectroscopy (FTIR) is a common technique. The infrared spectrum gathers spectral data over a wide range between $400\mathrm{cm}^{-1}$ and $8000\mathrm{cm}^{-1}$.

To measure a Fourier spectrum a Fourier spectrometer is required. The heart of such a spectrometer is a Michelson interferometer shown in figure 1.14.

The light of the source with intensity I_0 is split with a beamsplitter into a reflected and transmitted beam with same amplitude. Each part comes to a mirror where the beam is reflected back to the beamsplitter. The beams are again split into a reflective and a transmitted part. The detector measures a superposition of both beams. The distance between the beamsplitter and the mirror is denoted with L, if these lengths are different, the measured intensity contains a phase difference

$$\Delta\Phi = 2\frac{2\pi}{\lambda_0}\Delta L, \tag{1.11}$$

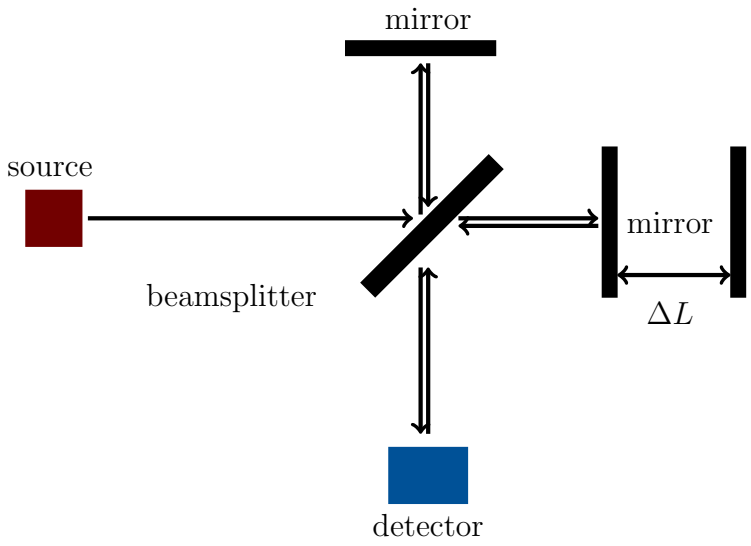

Figure 1.14: Schematic of a Michelson interferometer, the basic component of a Fourier spectrometer. The light from the source is split at the beamsplitter 1 : 1. The split light arrives at a mirror and is reflected back. The reflected light is again split and the superposition of the transmitted light is measured with a detector. The path difference ΔL causes a phase difference.

where λ_0 is the wavelength of the light source. The detected intensity is given by

$$I = I_0 \cos^2 \frac{2\pi \Delta L}{\lambda_0}. \tag{1.12}$$

The Michelson interferometer in a Fourier spectrometer allows to measure the auto-correlation of the optical signal. The power spectrum and the auto-correlation are connected via the Fourier transformation, given by the Wiener Kinchin theorem,

$$S(\omega) = \int_{-\infty}^{\infty} U(t)U^*(t+\tau)e^{\imath\omega\tau}d\tau. \tag{1.13}$$

In the sample compartment the light is focused via lenses onto the sample. The light passes trough the sample compartment and is focused onto the detector. An interferogram is obtained by varying the mirror position and recording the signal from the detector. The spectra is evaluated by a Fourier transformation of the interferogram.

Fourier spectroscopy of graphene

Fourier spectroscopy can be used to characterize graphene in an noninvasive manner. Yan et al. [30] demonstrated that through the analysis of the spectrum in the far and mid range, the number of layers, the doping level as well as carrier mobility and scattering rate can be evaluated. In the mid infrared an absorption

of 2.3% was measured according to interband transitions. Due to Pauli blocking this value is reached for energies greater $2 \cdot \mid E_F \mid$. Thus the doping level can be obtained. The number of layer can be figured out by evaluating the shape of the absorption in the mid infrared range. The carrier mobility as well as the scattering rate can be determined using the far infrared spectrum.

1.4.4 Mobility measurements

Due to its bandstructure, graphene has novel transport effects such as the ambipolar field effect and a minimum conductivity [6]. By measuring the I-V curve, the relation between source-drain current and gate voltage, the mobility, as well as the Dirac point can be evaluated. The technique requires contacts to measure the graphene. A graphene flake, deposited onto a piece of an oxidized silicon wafer, is structured by a lithographic process and electrically contacted with gold as schematically illustrated in the inset of figure 1.15.

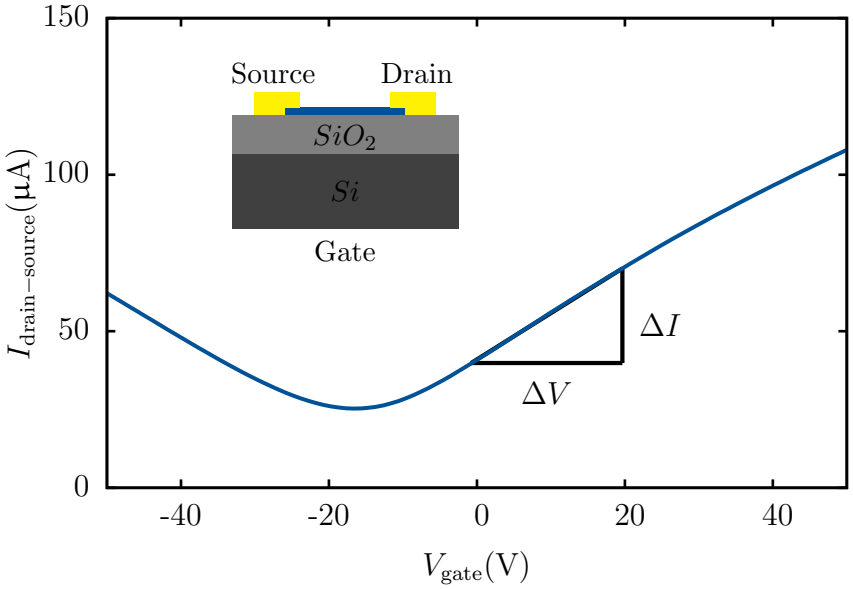

Figure 1.15: The carrier density can be tuned between the electron and hole regime by shifting the Fermi level with an applied gate voltage. The I-V curve is symmetric due to the ambipolar behavior of the carriers in graphene. The Dirac point is located at $-18V$, indicating doping. Theoretically, the carriers should disappear at the Dirac point. The non-vanishing conductance are due to electron-hole puddles and thermally generated carriers.

The Dirac point is located at -18V. Theoretically, the Dirac point is located at $0V$, the presence of impurities and defects cause this shift. The non-vanishing conductance arises from electron-hole puddles and thermally generated carriers. The carriers should disappear at the Dirac point. The charge carriers can be

tuned by shifting the Fermi level via a gate voltage between the silicon substrate and the graphene flake. The gate voltage induces charge carriers into the graphene. The relation between gate voltage and the charge carriers is

$$n = \frac{\epsilon_0 \epsilon V_g}{te}, \tag{1.14}$$

where e is the electron charge, t is the thickness of the silicon dioxide layer and ϵ is the relative permittivity of the silicon dioxide layer. Due to the change of charge carriers, the Fermi level shifts. Typically the mobility μ is estimated using Hall measurements. Another possibility is by taking the I-V curve into account. The calculation of the mobility from the I-V curve neglects the contact resistance, thus the mobility can only be roughly estimated. We assume a structure as depicted in the inset of figure 1.15 with a flake size of $A = L \times W$. The current between the source and drain contact is defined as

$$I_{\text{drain-source}} = nev_{\text{d}}W, \tag{1.15}$$

where n is the number of the electrons, e the electron charge v_{d} the drift velocity and W is the width of the graphene flake. The drift velocity depends on the electric field and on the mobility $v_{\text{d}} = \mu E$. The electric field is given by $E = U/L$, where U is the voltage between source and drain and L depicts the distance between the two contacts. Inserting this into equation 1.15, yields

$$\mu = \frac{L}{neW}\frac{I}{U}. \tag{1.16}$$

Using equation 1.14, we can obtain

$$\mu = \frac{L}{W}\frac{t}{\epsilon_0 \epsilon}\frac{\Delta G}{\Delta V_g}, \tag{1.17}$$

where $\Delta G = \Delta I / \Delta U$ is the electric conductance.

Chapter 2

Plasmonics

Nanophotonics has become an important research topic, as many interesting effects occur, when scaling down to the sub-wavelength range. Plasmonics is a major part of this field. Plasmons describe the interaction between electromagnetic waves and charged particles. Plasmons enable many applications like metamaterials, quantum optics, photovoltaics, photodetectors and biological sensing applications. Due to the two dimensional form of graphene, we focus on surface plasmons. A surface plasmon is a collective electron oscillation that occurs on an interface between two materials. This chapter describes the electromagnetic response of metals and the excitation of plasmons in metals to provide a theoretical background on plasmons. This knowledge is then used to describe surface plasmons in graphene.

A wave of charge density oscillations is referred to as a plasmon. In a neutral plasma with free positive and negative particles charge carrier density oscillations can occur. An example are metals, were the valence electrons are quasi-free particles moving around in the metal. The 'quasi-free' movement results from the force between the positive charged ion core and the electrons.

2.1 The Plasma model

The interaction of an electromagnetic field with metals can be described with the classical Maxwell equations. The optical properties of metals are described by the so called plasma model, where the electrons in the metal are assumed to be a gas of electrons which can freely move around against the fixed positive charged ion cores. The plasma model takes the band structure via an effective electron mass into account. Further effects between electrons and the lattice potential are neglected in the model [31].

The plasma model describes the interaction between an electric field $\mathbf{E}$ with the electrons in the metal. The motion of the electrons is described by

$$m\ddot{\mathbf{x}} + m\gamma\dot{\mathbf{x}} = -e\mathbf{E}. \tag{2.1}$$

During the oscillation, collisions at positive charged ions can occur. This is described by the typical collision frequency $\gamma = 1/\tau$, where τ denotes the relaxation time of the free electron gas.

Applying a harmonic external field in the form $\mathbf{E}(t) = \exp(-\imath\omega t)$, leads to

$$\mathbf{x}(t) = \frac{e\mathbf{E}_0}{m(\omega^2 + \imath\gamma\omega)} \exp(-\imath\omega t), \tag{2.2}$$

the particular solution of the equation of motion. The displaced electrons contribute to the polarization $\mathbf{P} = -ne\mathbf{x}$. Replacing x with the particular solution of the equation of motion and inserting into $\mathbf{D} = \epsilon_0\mathbf{E} + \mathbf{P}$, leads to

$$\mathbf{D} = \epsilon_0 \left(1 - \frac{\omega_p^2}{\omega^2 + \imath\gamma\omega}\right) \mathbf{E}, \tag{2.3}$$

with $\omega_p = ne^2/\epsilon_0 m$, the plasma frequency of the free electron gas. Comparing equation 2.3 with $\mathbf{D} = \epsilon_0\epsilon(\omega)\mathbf{E}$ gives the complex dielectric function of the free electron gas

$$\epsilon(\omega) = 1 - \frac{\omega_p^2}{\omega^2 + \imath\gamma\omega}. \tag{2.4}$$

The dielectric function can be split into a real and an imaginary part $\epsilon(\omega) = \epsilon_1(\omega) + \imath\epsilon_2(\omega)$, where the real part is

$$\epsilon_1(\omega) = 1 - \frac{\omega_p^2\tau^2}{1 + \omega^2\tau^2} \tag{2.5}$$

and the imaginary part is

$$\epsilon_2(\omega) = \frac{\omega_p^2\tau}{\omega(1 + \omega^2\tau^2)}. \tag{2.6}$$

Considering different frequency regimes, with respect to the collision frequency γ, either the real or the imaginary part of the dielectric function dominates the behavior of the metal. We will limit our considerations to frequencies below the plasma frequency, where metals retain their metallic character. For large frequencies, close, but beneath ω_p, the imaginary part of the dielectric function can be neglected, which lead to

$$\epsilon(\omega) = 1 - \frac{\omega_p^2}{\omega^2}, \tag{2.7}$$

the dielectric function of the loss less, thus undamped free electron gas. For low frequencies $\omega \ll \tau^{-1}$, metals mainly absorb.

2.1.1 Dispersion relation of the free electron gas

The dispersion relation describes the dependence of the frequency on the momentum and can be derived from the basic Maxwell equations. Combining the curl equations leads to the wave equation

$$\nabla \times \nabla \times \mathbf{E} = -\mu_0 \frac{\partial^2 \mathbf{D}}{\partial t^2}. \tag{2.8}$$

Assuming a harmonic electric field in the from $\mathbf{E}(t, \mathbf{x}) = \exp(-\imath\omega t + \imath \mathbf{k}\mathbf{x})$ with $\mathbf{k} = (k_x, k_y, k_z)^T$ denoting the wave vector, leads to

$$\mathbf{k}\,(\mathbf{k} \cdot \mathbf{E}) - k^2 \mathbf{E} = -\epsilon(\mathbf{k}, \omega) \frac{\omega^2}{c^2} \mathbf{E} \tag{2.9}$$

in the Fourier domain. In general one can distinguish between transversal and longitudinal polarized fields. The choice of the polarization influences the solution of the dispersion relation. Transverse waves satisfy $\mathbf{k} \perp \mathbf{E}$, thus $\mathbf{k} \cdot \mathbf{E} = 0$. The dispersion relation therefor can be written as

$$k^2 = \epsilon(\mathbf{k}, \omega) \frac{\omega^2}{c^2}. \tag{2.10}$$

According to the dispersion relation given in equation 2.10 and the dielectric function for negligible damping, equation 2.7 leads to

$$\omega^2 = \omega_p^2 + k^2 c^2, \tag{2.11}$$

the dispersion relation for transversal polarized fields of the free electron gas neglecting damping. Longitudinal waves satisfy $\mathbf{k} \parallel \mathbf{E}$, which leads to

$$\epsilon(\mathbf{k}, \omega) = 0. \tag{2.12}$$

Let us now have a look at the frequency regime $\omega > \omega_p$, the so called transparency regime of the free electron gas model [31]. Frequencies above the plasma frequency support propagation of transversal waves. Beneath the plasma frequency wave propagation of transversal electromagnetic modes is forbidden. Figure 2.1 depicts the dispersion relation of the free electron gas.

2.2 Surface plasmon polaritons

What is a surface plasmon polariton?
A confined evanescent electromagnetic wave propagating between a metal and a dielectric is referred to as surface plasmon polariton. The reason for this surface waves are the coupling of electromagnetic waves to oscillations of electron plasma at a metal/ dielectric interface. Surface plasmon polaritons propagation takes place on flat dielectric/metal interfaces. This effect can be described with the basic Maxwell equations.

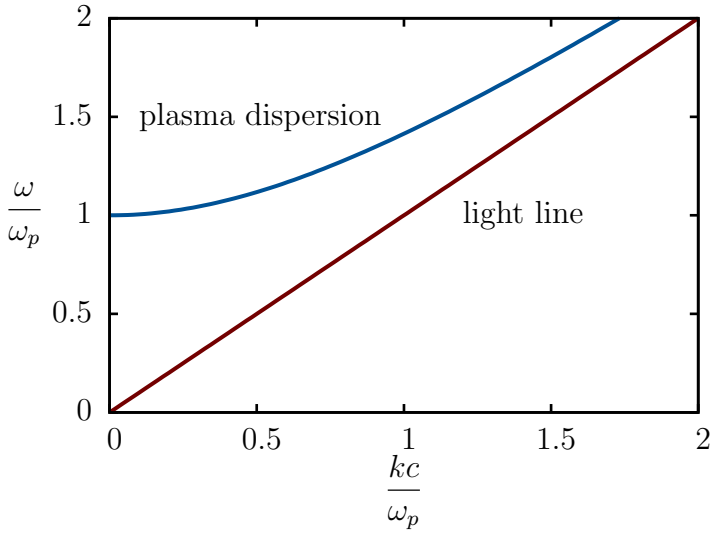

Figure 2.1: Dispersion relation of the free electron gas model. In the regime, where $\omega<\omega_p$, the propagation of transverse electromagnetic waves is forbidden. $\omega = \omega_p$ implicates that $\epsilon(\omega) = 0$, which is related to a longitudinal mode. Radiation into the metal is possible, if $\omega>\omega_p$ holds. This regime is referred to as transparency regime.

2.2.1 TE and TM surface waves

Starting point is again the wave equation 2.8. Assuming no external charge and current density ($\rho = 0$ and $\mathbf{J} = 0$) as well as isotropic permittivity in the range of the optical wavelength yields

$$\nabla^2\mathbf{E} - \frac{\epsilon}{c^2}\frac{\partial^2\mathbf{E}}{\partial t^2} = 0. \tag{2.13}$$

Assuming a harmonic electric field $\mathbf{E}(\mathbf{r}, t) = \mathbf{E}(\mathbf{r})\exp(-\imath\omega t)$, results in a wave equation in the Fourier domain in the following form

$$\nabla^2\mathbf{E} + k_0^2\epsilon\mathbf{E} = 0, \tag{2.14}$$

where $k_0 = \frac{\omega}{c}$ denotes the wave vector in vacuum. Assuming a one-dimensional problem in the Cartesian coordinate system. The electric field can be written as

$$\mathbf{E}(x, y, z) = \mathbf{E}(z)\exp(\imath\beta x). \tag{2.15}$$

The wave propagates in x direction. β is equal to k_x and depicts the wave vector of the traveling wave in propagation direction. The permittivity is assumed to be dependent only in the z-direction $\epsilon = \epsilon(z)$. Inserting equation 2.15 into equation 2.14 yields

$$\frac{\partial^2\mathbf{E}(z)}{\partial z^2} + (k_0^2\epsilon - \beta^2)\mathbf{E} = 0. \tag{2.16}$$

In order to define the field profile and the dispersion, the explicit expressions for **E** and **H** have to be derived from the two Maxwell equations which describe the dependence between electric and magnetic field. The explicit expressions for transverse magnetic (TM) modes are given as

$$E_x = -\imath \frac{1}{\omega \epsilon_0 \epsilon} \frac{\partial H_y}{\partial z} \tag{2.17}$$

$$E_z = -\frac{\beta}{\omega \epsilon_0 \epsilon} H_y \tag{2.18}$$

and

$$\frac{\partial^2 H_y}{\partial z^2} + (k_0^2 \epsilon - \beta^2) H_y = 0. \tag{2.19}$$

The other components H_x, H_z and E_y are zero.

For the transverse electric (TE) field where E_x, E_z and H_y are zero, the following set of equation holds.

$$H_x = \imath \frac{1}{\omega \mu_0} \frac{\partial E_y}{\partial y} \tag{2.20}$$

$$H_z = \imath \frac{\beta}{\omega \mu_0} E_y. \tag{2.21}$$

The wave equation for the TE mode

$$\frac{\partial^2 E_y}{\partial z^2} + (k_0^2 \epsilon - \beta^2) E_y = 0. \tag{2.22}$$

This set of equations permits us to describe surface plasmon polaritons.

2.2.2 Surface plasmon polaritons

We consider a flat interface between a metal and a dielectric material, as shown in figure 2.2. The dielectric material is described with the positive real permittivity ϵ_2 in the half space $z>0$. The adjacent halfspace $z<0$ is described by the frequency dependent permittivity $\epsilon_1(\omega)$. The metallic character requires $\Re(\epsilon_1(\omega))<0$. Assuming evanescent decay in z direction, we want to derive the solutions for a wave propagating at the interface between the two materials.

The transversal magnetic modes, described with equation 2.17 - 2.19 are the basis to derive the solutions for the field components. $H_y(z)$ follows from the wave equation, $E_x(z), E_z(z)$ are results of the explicit expressions derived from the Maxwell equations. For the halfspace $z>0$ the following set of equations can be

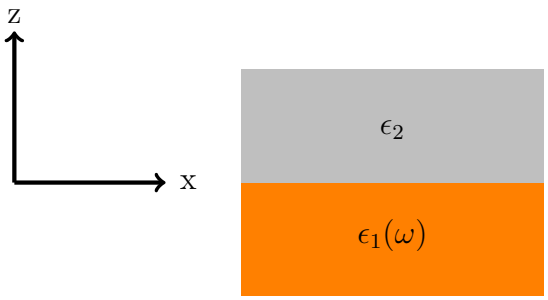

Figure 2.2: Sketch of an interface, existing of a dielectric material and metallic half space which are described by their permittivities.

derived

$$H_y(z) = A_2 \exp(\imath\beta x) \exp(-k_2 z), \tag{2.23a}$$
$$E_x(z) = \imath A_2 \frac{1}{\omega\epsilon_0\epsilon_2} k_2 \exp(\imath\beta x) \exp(-k_2 z), \tag{2.23b}$$
$$E_z(z) = -A_2 \frac{\beta}{\omega\epsilon_0\epsilon_2} \exp(\imath\beta x) \exp(-k_2 z) \tag{2.23c}$$

and for $z<0$

$$H_y(z) = A_1 \exp(\imath\beta x) \exp(k_1 z), \tag{2.24a}$$
$$E_x(z) = -\imath A_1 \frac{1}{\omega\epsilon_0\epsilon_1} k_1 \exp(\imath\beta x) \exp(k_1 z), \tag{2.24b}$$
$$E_z(z) = -A_1 \frac{\beta}{\omega\epsilon_0\epsilon_1} \exp(\imath\beta x) \exp(k_1 z). \tag{2.24c}$$

where $k_{1,2}$ denotes the wave vectors perpendicular to the interface at $z = 0$ in direction of the metal (1) and the dielectric (2). This results from the assumption that the field decays evanescently in z-direction.

At the interface $z = 0$, continuity for H_y and E_x is required. Thus the following conditions have to be fulfilled

$$A_1 = A_2, \tag{2.25a}$$
$$\frac{k_2}{k_1} = -\frac{\epsilon_2}{\epsilon_1}. \tag{2.25b}$$

And as a consequence of equation 2.19

$$k_1^2 = \beta^2 - k_0^2\epsilon_1, \tag{2.26a}$$
$$k_2^2 = \beta^2 - k_0^2\epsilon_2 \tag{2.26b}$$

have to be fulfilled. Combining these conditions leads to the dispersion relation of waves propagating on a flat interface between a metal and a dielectric material

$$\beta = \frac{\omega}{c}\sqrt{\frac{\epsilon_1\epsilon_2}{\epsilon_1+\epsilon_2}}. \tag{2.27}$$

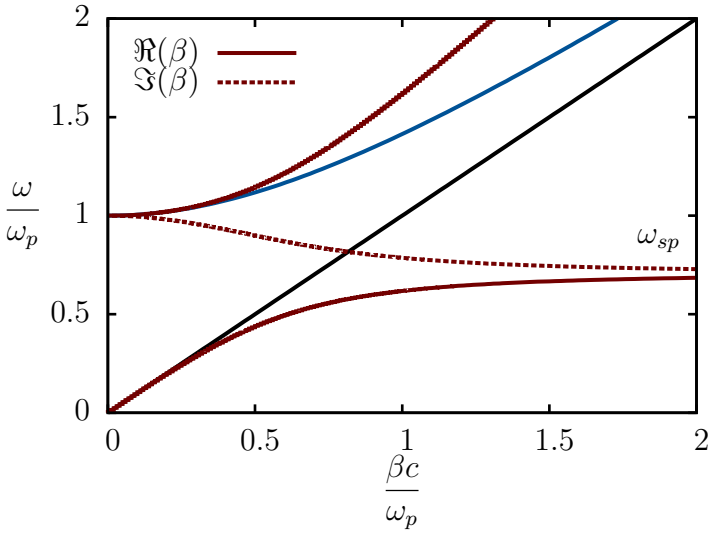

Figure 2.3: Illustration of the dispersion relation of a surface plasmon polariton. The half spaces consists of metal, which is described with the free electron gas model and air (red). The blue curve limits the transparency range of the metal, where the radiation into the metal is possible.

Figure 2.3 displays equation 2.27 assuming the dielectric material to be air ($\epsilon_2 = 1$) and the plasma model without damping for the metal as given in equation 2.7.
Depending on the real and imaginary part of the dispersion relation β, three domains of wave propagation have to distinguished. Figure 2.3 depicts the real and imaginary part of the dispersion relation as well as the plasma dispersion of the free electron gas and the light line of air. In the transparency range $\omega > \omega_p$, the plasma supports transversal waves in the metal. In the range between the plasma dispersion and the light line, β is purely imaginary. Hence, the waves decays evanescently in x direction. In this range wave propagation is forbidden. For values beneath the light line propagation of a wave in x direction is possible. The characteristic surface plasmon frequency can be obtained for large values of β as

$$\omega_{sp} = \frac{\omega_p}{\sqrt{1+\epsilon_2}}. \tag{2.28}$$

In the case of negligible damping $\Im(\epsilon_1(\omega)) = 0$, β goes to infinity as the frequency approaches the characteristic surface plasmon frequency ω_{sp}. The mode acquires

electrostatic character and is therefore known as surface plasmon [31]. The requirement for negligible damping is satisfied in metals such as gold or silver. Figure 2.4 illustrates the real and imaginary part of the permittivity of gold and silver.

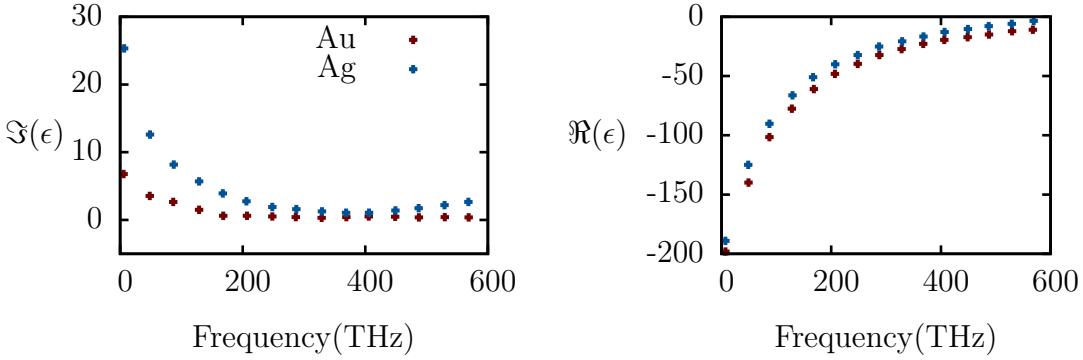

Figure 2.4: Experimental data of the real and imaginary part of the permittivity of gold (red) and silver (blue). Data taken from [32].

Taking k_1 and k_2 into account, it is possible to figure out the conditions for the wave vectors to obtain a surface plasmon. Above the plasma frequency ω_p both wave vectors k_1 and k_2 are real as shown in figure 2.5. This case describes a electromagnetic wave, which propagates in z. If β is also real, this reveals a electromagnetic wave propagating in z and x direction. A imaginary β results in a wave which is damped in x direction an propagates in z direction. If k_1 and k_2 imaginary and β is real an electromagnetic wave bound to the interface occurs, referred to as surface plasmon.

The previous description holds for transversal magnetic (TM) waves. For a transversal electric (TE) field the field components for $z>0$ are given as

$$E_y(z) = A_2 \exp(\imath\beta x) \exp(-k_2 z), \tag{2.29a}$$

$$H_x(z) = -\imath A_2 \frac{1}{\omega\mu_0} k_2 \exp(\imath\beta x) \exp(-k_2 z), \tag{2.29b}$$

$$H_z(z) = A_2 \frac{\beta}{\omega\mu_0} \exp(\imath\beta x) \exp(-k_2 z) \tag{2.29c}$$

and for $z<0$

$$E_y(z) = A_1 \exp(\imath\beta x) \exp(k_1 z), \tag{2.30a}$$

$$H_x(z) = \imath A_1 \frac{1}{\omega\mu_0} k_1 \exp(\imath\beta x) \exp(k_1 z), \tag{2.30b}$$

$$H_z(z) = A_1 \frac{\beta}{\omega\mu_0} \exp(\imath\beta x) \exp(k_1 z). \tag{2.30c}$$

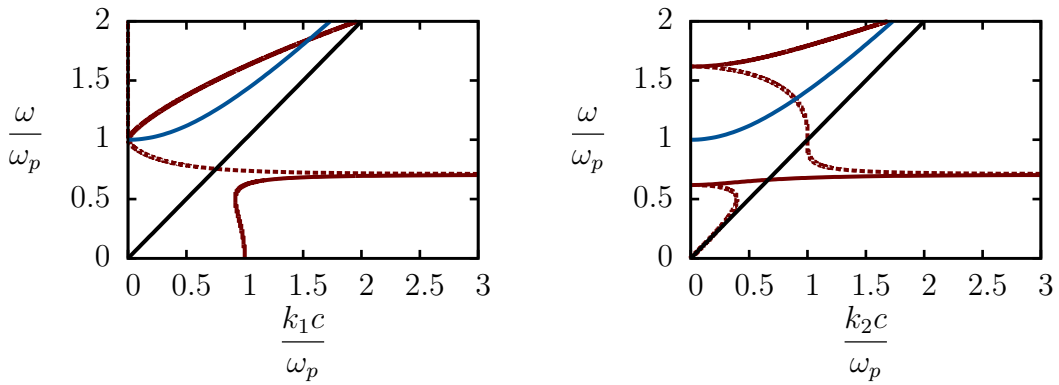

Figure 2.5: Illustration of the dependence of the plasma dispersion on the wave vectors k_1 and k_2 perpendicular to the surface. Assuming $\Re(\beta)>0$ and $\Re(k_1, k_2)<0$, a surface plasmon can be excited. Above the plasma frequency the wave vectors are both real which results in a electromagnetic wave propagating in x and z direction with a real wave vector β. An evanescently damped wave in x direction propagating in z direction can occur, if β is imaginary.

Continuity at the interface $z = 0$ results in

$$A_1 = A_2, \tag{2.31a}$$
$$k_1 A_1 = -k_2 A_2. \tag{2.31b}$$

Resulting in

$$A_1(k_1 + k_2) = 0. \tag{2.32}$$

Confinement at the interface requires $\Re(k_1)>0$ and $\Re(k_2)>0$ [31]. Thus condition 2.32 is only fulfilled if $A_1 = 0$. If $A_1 = A_2 = 0$ propagation of a surface plasmon is not possible. Therefore no surface modes exist for transversal electric polarization.

2.2.3 Excitation of plasmons at planar interfaces

In principle a surface plasmon polariton is a wave propagating at the interface between a metal and a dielectric material. We assume a wave confined at an interface between a metal and a dielectric material. The wave decays evanescent into both half spaces and propagates along the surface. Figure 2.3 depicts the dispersion relation of a metal/ air interface and the light line of air. To excite a surface plasmon, light with proper frequency and momentum has to be provided. For small frequencies and wave vectors, the light line is close to the dispersion relation, thus $\beta \approx k$ and a plasmon can be excited. At higher frequencies the excitation of a surface plasmon polariton on planar surface is not allowed due to

the momentum mismatch between the incoming light and the surface plasmon polariton. To overcome this mismatch certain phase matching techniques were developed. A possibility to couple light into a surface plasmon polariton was revealed by Otto, Kretschmann and Raether in 1968 using prisms. In 1902 Wood observed coupling of light into a surface plasmon by structuring the metal surface as a grating [31].

Prism coupling

The excitation of a surface plasmon polariton on a planar metal/air interface is not allowed due to the momentum mismatch between air and the plasmon. Hence, the part of wave vector of the incoming light parallel to the surface has to be changed so that phase matching occurs. To overcome this, it is possible to change the dielectric material to a material with higher permittivity as air. The influence of the material on the momentum is given as

$$k = \frac{\omega}{c}\sqrt{\epsilon}. \tag{2.33}$$

The momentum changes for the same frequency to a higher values. Thus using for example a prism made out of glass ($\epsilon \approx 4$) modifies the momentum as illustrated in figure 2.6. Coupling of the incoming light into a surface plasmon polariton is expected due to the intersection point between dispersion relation and modified light line.

What we now know, is that we have to use a material with higher permittivity to increase the momentum of the incoming light. But how to couple into the surface plasmon polariton? The answer was given by Otto, Kretschmann and Raether. They used the *Attenuated Total Reflection (ATR)* to couple into a surface plasmon polariton.

Assuming an air/glass interface as shown in figure 2.7 ,where the light with the momentum k_0 impinges under an angle θ.

The momentum parallel to the interface is given as

$$k_{x,glas} = k_0\sqrt{\epsilon_{\text{glass}}}\sin(\theta). \tag{2.34}$$

The momentum perpendicular to the interface can be written as

$$k_{\text{z,air}} = \sqrt{k_0^2 - k_{\text{x,glass}}^2} = \sqrt{k_0^2 - k_0^2\epsilon_{\text{glass}}\sin(\theta)}. \tag{2.35}$$

If the angle of the incoming light θ becomes equal to the angle of total reflection, the incoming light becomes totally reflected back into the glass and the momentum $k_{z,air}$ becomes imaginary. The angle of total reflection depends on the permittivities of the surrounding media and can be derived as

$$\theta_{\text{total}} = \arcsin\left(\frac{\epsilon_{\text{air}}}{\epsilon_{\text{glass}}}\right). \tag{2.36}$$

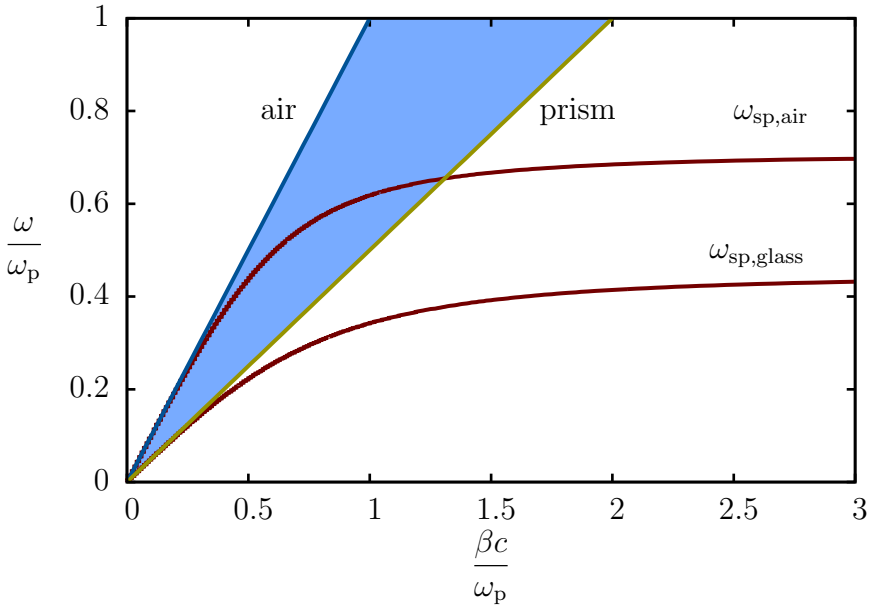

Figure 2.6: Dispersion relation (red) of a metal/air interface. By using a prism the light line is shifted to higher frequencies (yellow). Between the two light lines (blue area), it is possible to excite a surface plasmon polariton.

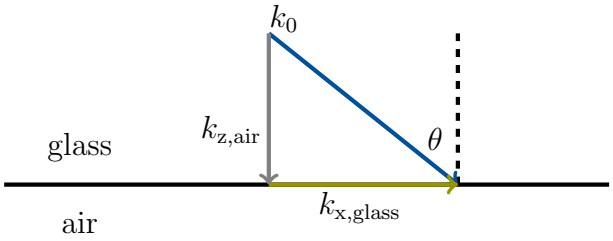

Figure 2.7: Momentum distribution on a glass/air interface. The momentum $k_{\mathrm{z,air}}$ perpendicular to the interface becomes complex, if the angle of the incident light is greater than the angle of total reflection. Thus impinging light gets totally reflected into the glass. The field of the incoming light wave decays in the air evanescently.

At the surface, the reflected light decays evanescently into the air. This evanescent light has a momentum which is modified by the glass. Due to the glass, the momentum is changed so that phase matching can occur. Hence, it is possible to couple into a surface plasmon polariton. This effect is the so called *Attenuated total reflection*. Whether phase matching has occurred and the light couples to a surface plasmon polariton can be found out by detecting the reflected light. If the reflected light is attenuated, one can assume coupling.

Figure 2.8 a) depicts the so-called Otto configuration. The metal surface is brought close to the glass/air interface, so that the evanescent field can couple

into a surface plasmon polariton at the metal/air interface. In the Kretschmann configuration, shown in figure 2.8 b), the metal surface is directly deposited onto the glass prism. The evanescent field from the prism couples through the metal into a surface plasmon polariton. This effect is referred to as optical tunneling effect[33].

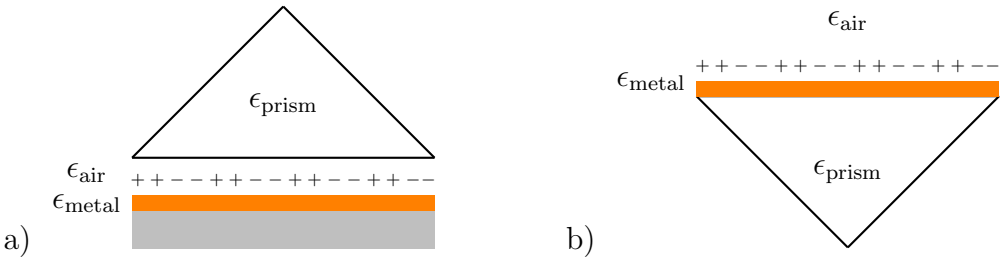

Figure 2.8: Illustration of prism coupling with a Otto configuration a) and a Kretschmann configuration b).If the incident light impinges with an angle larger then the angle of total reflection, the parallel component of the momentum becomes equal to the momentum of the surface plasmon polariton. As a result, the incoming light can couple to the surface plasmon polariton.

The intensity of the reflected light indicates coupling of light into a surface plasmon polariton. If coupling occurs the reflected light is attenuated. By changing the angle and the wavelength of the incident light and measuring the reflected intensity it is possible to determine the dispersion of the plasmon frequency.

Grating coupling

The concept of using a grating is to match the parallel part of the momentum from the incident light to the plasmon. The metal surface is patterned either with a grating, grooves or holes with a lattice constant a. Figure 2.9 depicts such a grating. A electromagnetic wave couples into the surface plasmon polariton if the phase matching condition

$$\beta = k\sin(\theta) + \nu\frac{2\pi}{a} \tag{2.37}$$

is fulfilled, where $\nu = \pm 1, 2, 3 \ldots$. Figure 2.10 depicts the dispersion relation for a structured metal surface.

The red curve depicts the dispersion relation of a planar interface. The yellow curves depicts the dispersion relation for a groove structured surface. A surface plasmon polariton can be excited within the line cone (blue).

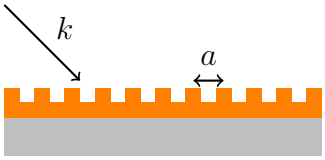

Figure 2.9: Illustration of a grating structure. If the momentum of the deflected light fulfills the phase matching condition, a surface plasmon polariton can be excited. The shape of the structured surface can influence the propagation direction. The effect of phase matching can also occur if the surface has a certain roughness.

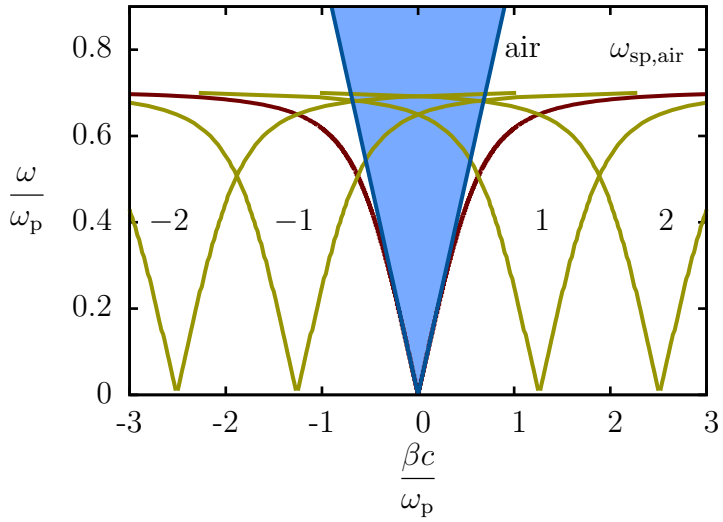

Figure 2.10: Illustration of the dispersion relation of a groove structured metal surface. Due to the periodic change of the momentum from the incident light, phase matching can be achieved. The red curve depicts the dispersion relation of a flat metal surface. Structuring the surface with grooves, the dispersion relation becomes convoluted with multiples with the grating period.

2.3 Plasmons in graphene

Metals such as gold or silver are common materials for plasmonic structures. Relatively high losses and the nontunability, once the geometric structure is fixed, limit the range of applications [34]. Due to the high electron mobility in graphene, the optical losses are much smaller than in commonly used metals. Furthermore, graphene has the ability to tune the plasmon resonance by adjusting the Fermi level via electrical or chemical doping. This illustrates the potential of graphene for surface plasmon nanostructures.

2.3.1 Dispersion relation of graphene

We assume a graphene sheet with the conductivity $\sigma(\omega)$ surrounded by two dielectric materials with the permittivities $\epsilon_{1,2}$, as shown in figure 2.11. We want to derive the dispersion relation to find the conditions of plasmon excitation on graphene. The graphene sheet can be seen as a conductor, where free charges can couple to electromagnetic waves.

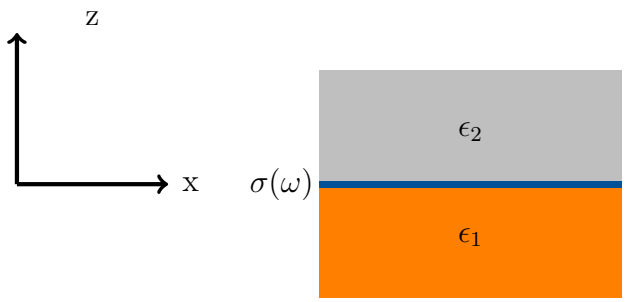

Figure 2.11: Graphene sheet with conductivity $\sigma(\omega)$ between two half spaces with different permittivities $\epsilon_{1,2}$.

Beginning with the general boundary conditions

$$\mathbf{n} \times [\![\mathbf{E}]\!] = \mathbf{0}, \tag{2.38a}$$
$$\mathbf{n} \cdot [\![\mathbf{B}]\!] = 0, \tag{2.38b}$$
$$\mathbf{n} \times [\![\mathbf{H}]\!] = \mathbf{K}, \tag{2.38c}$$
$$\mathbf{n} \cdot [\![\mathbf{D}]\!] = \sigma \tag{2.38d}$$

and assuming that the graphene sheet lies at $z = 0$ in the xy - plane, a current density $\mathbf{J}_s$ (current per unit length) and a charge density ρ_s (charge per unit area) leads to the boundary condition for the interface shown in figure 2.11

$$\mathbf{E}_{1t} = \mathbf{E}_{2t}, \tag{2.39a}$$
$$B_{1n} = B_{2n}, \tag{2.39b}$$
$$\mathbf{H}_{1t} - \mathbf{H}_{2t} = \mathbf{J}_s \times \mathbf{n}, \tag{2.39c}$$
$$D_{n1} - D_{2n} = \rho_s. \tag{2.39d}$$

Assuming graphene as a two dimensional metal with frequency dependent $\sigma(\omega)$, the current density $\mathbf{J}_s = \sigma(\omega)\mathbf{E}_t$, where $\mathbf{E}_t$ describes the electric field in the xy-plane. We now look at the transversal electric and transversal magnetic modes. The solutions for the TM modes at such an interface are given by the equation set 2.24 and 2.23 for both half spaces. Due to its two dimensional form, graphene can be considered via the boundary conditions [35] . For transversal magnetic waves, E_x, E_z and H_y nonzero. The boundary conditions for an isotropic $\sigma_{xx} = \sigma_{yy} = \sigma$

system are

$$E_{1x} = E_{2x}, \tag{2.40a}$$
$$H_{1y} - H_{2y} = \sigma E_x, \tag{2.40b}$$
$$\epsilon_1\epsilon_0 E_{1z} - \epsilon_2\epsilon_0 E_{2z} = \rho_s. \tag{2.40c}$$

Inserting the solution from 2.24 and 2.23 into the boundary conditions 2.40 results in

$$E_{1x} = E_{2x}, \tag{2.41a}$$
$$H_{1y} = -\frac{k_1\epsilon_2}{k_2\epsilon_1} H_{2y}, \tag{2.41b}$$
$$H_{1y} = H_{2y} - \frac{\sigma}{\mu_0} E_{1x}. \tag{2.41c}$$

The dispersion relation can be obtained by inserting equation 2.41(b) into 2.41(c) and replacing $E_{1x} = \imath\dfrac{1}{\omega\epsilon_0\epsilon_1} k_1 H_{1y}$ which yields

$$1 + \frac{k_1\epsilon_2}{k_2\epsilon_1} + \imath\sigma\frac{k_1}{\omega\epsilon_0\epsilon_1} = 0. \tag{2.42}$$

With the results from equation 2.19, the wave vectors are

$$k_1^2 = \beta^2 - k_0^2\epsilon_1, \tag{2.43a}$$
$$k_2^2 = \beta^2 - k_0^2\epsilon_2. \tag{2.43b}$$

Assuming $\sigma(\omega))$ is dominated by Drude absorption and neglecting scattering [35] results in

$$\frac{\epsilon_1}{\sqrt{(\hbar c\beta)^2 - \epsilon_1(\hbar\omega)^2}} + \frac{\epsilon_2}{\sqrt{(\hbar c\beta)^2 - \epsilon_2(\hbar\omega)^2}} = \frac{4\alpha E_F}{(\hbar\omega)^2}. \tag{2.44}$$

A straight forward method to describe the dispersion relation was given in [36] with the semi-classical model. If $\beta \gg \frac{\omega}{c}$, the dispersion relation can be written as

$$\beta \approx \epsilon_0\frac{\epsilon_1 + \epsilon_2}{2}\frac{2\imath\omega}{\sigma(\omega,\beta)}. \tag{2.45}$$

Assuming that the conductivity of graphene can be described via the plasma model [36], yields

$$\beta(\omega) = \frac{\pi\hbar^2\epsilon_0(\epsilon_1 + \epsilon_2)}{e^2 E_{\mathrm{F}}}\left(1 + \frac{\imath}{\tau\omega}\right)\omega^2. \tag{2.46}$$

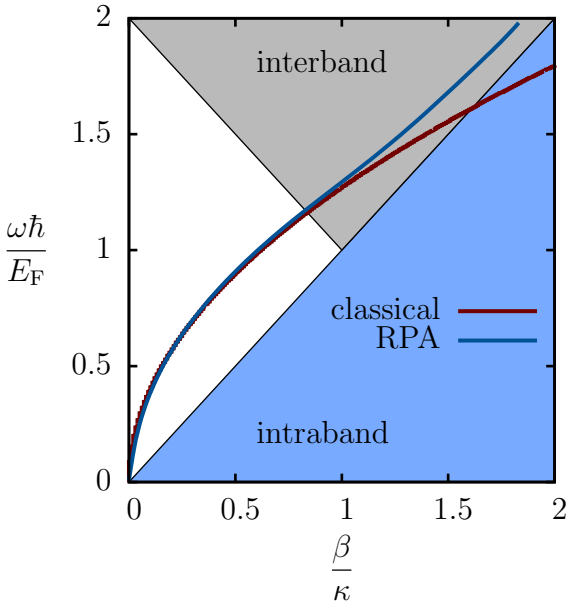

Figure 2.12: Dispersion relation related to the semi-classical model including electron impurity, electron defects and electron-phonon scattering (red). The blue curve depicts the solution the random phase approximation approach as reported in Jablan et. al.[36]. The grey area depicts the interband absorption and the blue area depicts the range of intraband absorption. The permittivities for each half space were chosen to be $\epsilon_1 = 4$ and $\epsilon_2 = 1$, corresponding to an air/ silicon interface with graphene in between.

Equation 2.46 describes the dispersion relation at zero temperature for highly doped graphene, taking losses due to electron impurities, electron defects and electron-phonon scattering into account.

The semi-classical model agrees very well beneath the interband threshold as shown in figure 2.12. At higher frequencies interband losses have to be taken into account. Jablan et. al [36] revealed that large plasmon losses occur in the interband regime (grey area), due to excitation of electron hole pairs. The calculation of losses is performed within the framework of random - phase approximation and number conserving relaxation time approximation. The dispersion relation is depicted in figure 2.12 (blue). A detailed description of the dispersion relation is given in Ref. [36].

Chapter 3

Experimental

CVD graphene was structured using electron beam lithography and reactive ion etching. Grating structures with grating periods of 250 nm and 440 nm and a fill factor of 50 % were fabricated. The samples were characterized with Raman spectroscopy to evaluate the number of layers, structural defects and the doping level. The plasma resonances were measured with a Fourier spectrometer. This chapter contains the fabrication and characterization methods and the results.

3.1 Processing techniques

To fabricate graphene gratings several processes are required. Due to the grating period beyond the resolution of conventional optical lithography tools, electron beam lithography was used for patterning, followed by reactive ion etching. After structuring the graphene, a gold aperture was fabricated to reduce the background signal, improving the signal to noise ratio in the measurements. These fabrication steps are described in the following part.

3.1.1 Electron beam lithography

Structures, beyond the resolution of conventional optical lithography, can be fabricated using electron beam lithography. The applications reach from mask making to research sub-nanometer electronics. In the $1960's$ the first electron beam lithography machines were built, based on scanning electron microscopes (SEM). This lithography technique can be used for a variety of substrate materials and provide the opportunity of structuring in the nanometer regime. The main drawbacks of electron beam lithography are the expensive mechanical structure and a long process time.

An electron beam lithography machine consists of a column, responsible for beam forming and controlling, a chamber including a stage to move the sample, and a computer which enables handling. The part which forms and controls the beam is referred to as column. Figure 3.1 depicts a schematic of such a column.

The chamber is positioned underneath the column, including the states which allows the user to move the sample and treat more than one sample. Vacuum is required during the work in the chamber, thus a load lock is used to load and unload samples. The system is controlled via a computer, where a software platform allows communications and enables the user to load or unload samples, setting exposure jobs or aligning and focusing.

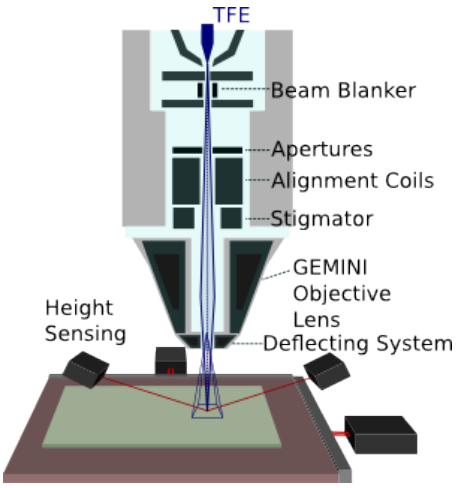

Figure 3.1: Sketch of an electron beam lithography tool. Taken from [37].

A typical column consists of an electron source, lenses, a beam deflecting mechanism, a beam blanker, a stigmator, apertures and alignment system and an electron detector. The electron source provides electrons either by emitting from a conducting material or by heating the conducting material until the electrons have enough energy to overcome the work function barrier. Another possibility to generate electrons, is to provide them by applying a strong electric field that the electrons can tunnel through the barrier. The emission properties are typically controlled via electrodes. An important property of these sources is the stability over the time. Thermal sources are less sensitive to the environment and thus stability over several months can be achieved[38]. The provided electrons have to be focused, with electrostatic or magnetic forces. Electron lenses behave similar to optical lenses. Electronic lenses are only able to converge the electron beam. Such a lens using magnetic forces is based on two circularly symmetric iron poles with copper winding's. The magnetic field bears a force on the electrons toward the optical axis, thus the beam gets focused. An aperture is in principle a small hole were the beam passes through and is thereby shrunk. Apertures are used in several ways in a column. The angle of beam convergence and the beam current is defined by an aperture. The scattering aperture is used to block any strayed electrons from the electron source without effecting the beam.

The position of the electron beam is controlled via deflectors. Deflectors can be realized either electrostaticly or magnetically. Typically, electrostatic deflection

is used because of the much higher speed. Beam blanking mechanisms, realized by deflectors, are used to turn the beam on and off. The beam is deflected away from the straight forward path, thus no electrons move through the apertures. Due to imperfection of the beam path, a stigmator has to be used for correction. Imperfection such as astigmatism, is corrected by a special electrostatic lens. The detector is usually realized by a silicon solid state detector mounted on the end of the third reduction lens. Back scattered electrons with an high energy content are measured because they can penetrate through the resist. Electrons with an low energy content are obscured by the resist[38].

Proximity effect

Adjacent areas are indirectly exposed by scattered electrons. The amount of back scattered electrons depends on the incident beam energy [39] and the thickness of the resist. If the electrons back scattered from the substrate contribute a exposure of the resist, the pattern is larger as required, this is referred to as Proximity effect. The proximity effect can be corrected by modifying the exposure dose or correcting the dimensions of the pattern which has to be exposed.

3.1.2 Reactive ion etching

Plasma etching is based on the reaction of ionized molecules with a solid, that react with each other and form a volatile product. The gas phase for the etching environment is generated from a feed gas which is discharged by electron-impact dissociation/ionization [40]. Etch gases such as Argon, Oxygen, SF6, SiCl4 and Cl2 are feed into a chamber at low pressure and a radio frequency signal is passed trough them. Due to the radio frequency signal, the gas molecules are cracked, leading to a plasma containing neutrals, ions, radicals and electrons. The wafer is typically placed on a radio frequency driven electrode, so that a voltage difference between the substrate and the plasma occurs. Hence, the reactive etch species is accelerated towards the substrate and reacts with the substrate. Due to the acceleration directed towards the substrate reactive ion etching causes etching mainly in the vertical direction. The volatile etch products diffuse from the surface back into the plasma and are pumped out.

Additionally, a inductively coupled plasma (ICP) can be used to enhance the anisotropy. The ICP systems increases the etch rate due to generation of additional ions, resulting in a more anisotropic etch process.

3.1.3 Optical lithography

Optical lithography or photo lithography is a basic process in the semiconductor industry to pattern substrates, metal films for micro-fabrication. Ultraviolet light is used to transfer geometric structures from a mask onto a substrate coated with

resist. Structures down to a few µm can be fabricated through optical lithography. The substrate have to be cleaned before spin coating to remove residuals. A flat surface is required to get a good quality of the structured resist. The following steps describe the standard optical lithography process using positive resist.

a) Liquid resist is spin-coated on the sample at around 1200 rpm to 4800 rpm for 30 s to 60 s to obtain a homogeneous resist layer. According to the required resist thickness the parameters of the spinner have to be varied. After deposition of the resist onto the substrate, the sample has to be baked, to remove remaining solvents.

b) In the next step the sample is exposed. This can be done with several techniques, depending on the wavelength of the light and the mask position. Typically, ultraviolet light is used to change the chemical composition of the resist. Depending on the resist, it becomes soluble (positive) or non-soluble (negative) after exposing.

c) The sample is developed in a alkaline solution. The soluble part is removed with this process step. The developing process is stopped, when the sample is put into water.

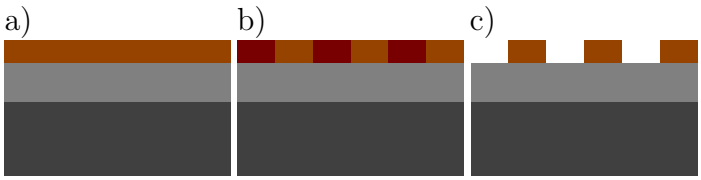

Figure 3.2: Illustration of a lithographic process using a positive resist. **a)**spin coating of the resist **b)** exposing of the wanted pattern **c)** pattern after developing

Trough a post bake and a second exposure, the chemical properties of the resist become reverse. This process is referred to as image reversal process. The common resist is spin coated, heat out an than exposed as a positive resist. The properties of the photo resist become changed by a second post bake. The sample has to be flood exposed leading to solubility of the unexposed structures as illustrated in figure 3.3.

The advantage of a image reversal or negative process are the overhanging flanks,so that a lift off if deposited materials is easier to obtain.

3.1.4 Metalization

Metalization is an important process in the fabrication of microelectronic devices. Beside sputtering systems, where the source material is bombarded energetic argon ions, metals can be evaporated. In this work, a electron beam vapor deposition tool

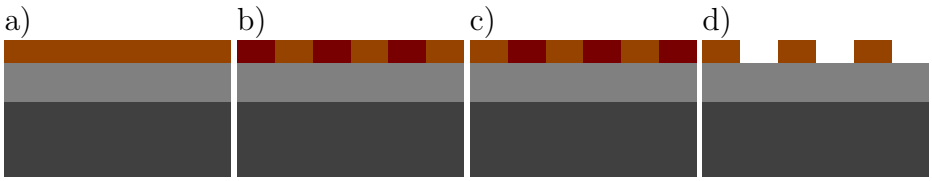

Figure 3.3: Illustration of an image reversal process. **a)**spin coating of the resist **b)** negative of the wanted pattern **c)** reverted properties of the resist after post bake and flood exposure **d)** developing

was used. This technique uses an electron beam to transform a target material into volatile phase. A charged tungsten filament delivers electrons which are directed by an magnetic field to the target anode. The metal in the target is heated up until it changes to volatile phase, the atoms precipitate into solid form when they reach a surface with lower temperature. The electron beam is accelerated to a high kinetic energy and is directed towards the target materials through a magnetic field. This technique enables well controllable deposition rates at relatively low substrate temperatures. The layer quality is much better in comparison to sputtered layers. Reducing imperfections and impurities the chamber is pumped to 1×10^{-7} Pa. The target material is heated up by converting the kinetic energy of the electrons into thermal. Figure 3.4 depicts the process steps of metalization.

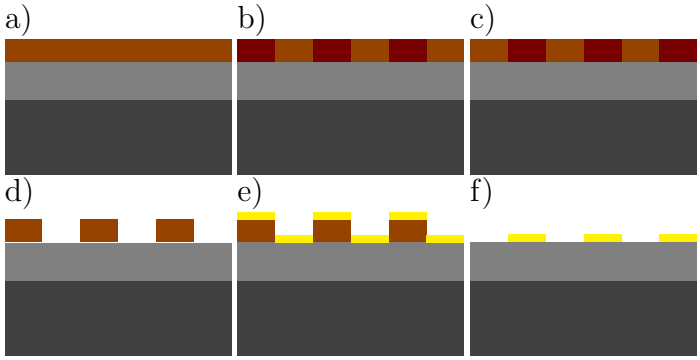

Figure 3.4: Illustration of the metalization process. **a)**spin coating of the resist **b)** negative of the wanted pattern **c)** reverted properties of the resist after post bake and flood exposure **d)** developing **e)** metalization **f)** sample after lift off

Various types of metals can be deposited onto substrates with this technique. The metalization via evaporation allows deposition rates lower than 1 nm/s, thus the layer thickness is well controllable.

3.2 Sample preparation

Graphene grown with chemical vapor deposition on copper was used in this work. The graphene was transferred onto a silicon substrate with 300 nm silicon dioxide

on it. Two samples with different grating periods were fabricated using electron beam lithography. The background signal was reduced by fabricating a gold aperture, thus the signal to noise ration was improved.

3.2.1 Graphene patterning

The graphene was patterned, using electron beam lithography. The electron beam lithography tool used in this work is a Raith e-LiNE electron beam lithography tool. A thermal field emission filament was used as source. The stage has a travel range of 100 mm × 100 mm and is controlled with a laser-interferometer with an accuracy of about 2 nm. The column voltage can be changed from 100 eV to 30 keV. The electron beam current is controlled through the aperture size. The system allows six apertures: 7.5 µm,10µm, 20 µm, 30 µm, 60 µm, 120 µm. Large area patterns are typically divided into smaller writing fields which are stitched together, depending on the resolution[41].

Grating structures with a size of 2 mm × 2 mm and a grating period of 250 nm and 440 nm and a fill factor of 50 % were written using electron beam lithography. The PMMA 679.904 was spin coated on the sample for 35 s with 4000 rpm. A column voltage of 10 keV and an aperture size of 30 µm resulting in a current around 150 pA were used. After the writing process, the samples were developed in $AR600-56$ for 30 s and put into isopropanol for 60 s to stop the developing. After patterning the resist on the sample, the uncovered graphene was etched away with an reactive ion etch process. The parameters used for dry etching were 15 s, 20 sccm oxygen flow rate and 50 W RF power under a temperature of 30 °C. Due to the proximity effect, the first fabricated structures did not have 50 % fill factor. Thus, a series of varying dose factor and a constant grating period were fabricated. By varying the dose factor we figured out that dose factors greater than one broadens the written bar while dose factors smaller than one do not expose the complete resist in the vertical direction. The other possibility to overcome the proximity effect is to vary the dimensions. Therefore a series with varying bar size, but constant grating period and constant dose factor of one were fabricated, as shown in figure 3.5.

The bar size was varied from 80 nm to 190 nm to get a bar size of 220 nm after the etching process. In a second step, the bar size was fine tuned from 130 nm to 145 nm. Due to the fabrication, the fill factor of the gratings increases approximately by 20%. Thus, grating bars were written with a size of 130 nm to achieve a size of 220 nm (grating period 440 nm) on the fabricated structure. Figure 3.6 shows SEM pictures of the fabricated gratings with a period of 250 nm and 440 nm.

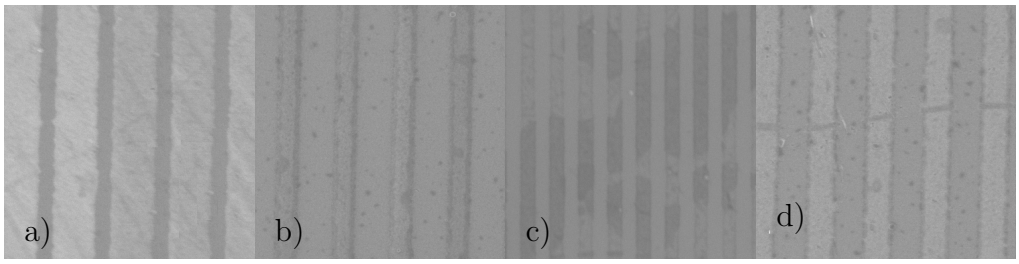

Figure 3.5: SEM pictures of a series with varying fill factor. Due to the proximity effect, the fill factor varies. Thus, a series of gratings with different fill factor were fabricated, to figure out the proper writing dimensions. a) grating with a period of 440 nm and 26 % fill factor b) grating with a period of 440 nm and 39 % fill factor c)grating with a period of 440 nm and 50 % fill factor d) grating with a period of 440 nm and 57% fill factor.

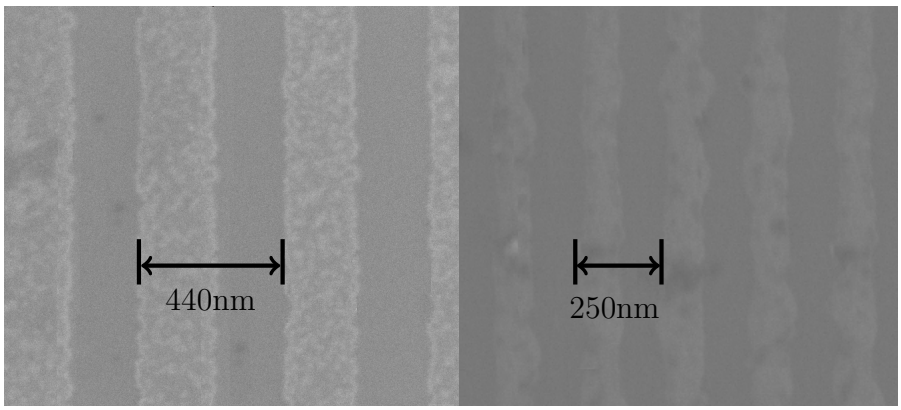

Figure 3.6: Scanning electron microscope images of the groove structured graphene. Gratings with different grating periods were fabricated. The right picture shows a grating with 250 nm period. The left picture depicts a grating with a period of 440 nm. Both gratings were fabricated with 50 % fill factor.

3.2.2 Aperture fabrication

A gold aperture surrounding the graphene grating was fabricated to reduce the background stray light, thus improving the signal to noise (SNR) ratio. Due to the aperture, the excitation light can only pass through the grating, resulting in a better SNR . The gold aperture was fabricated using optical lithography to define the opening. 120 nm gold was then deposited onto the sample. The thickness of the gold layer has to larger than the penetration depth of light in the mid infrared [32].

Optical lithography

The aperture was defined using a laser writer lithography tool at the ZMNS cleanroom. This lithography tool enables patterning of the photo resist without a

mask. The structure can be drawn in Autocad and transferred to the resist. For the transfer of the aperture an image reversal process was used due to the overhanging flanks which enable a much better lift-off of the gold. The sample was cleaned in acetone and isopropanol before spin coating. AZ5214 photo resist was spinned at 4000 rpm for 35 s. After 1 min on the hotplate at 100 °C most of the solvents were removed. The 1.9 mm × 1.9 mm rectangle was patterned using the laser writer lithography tool. After 2 min at 120 °C the sample was flood exposed for 15 s, changing the properties of the resist. The sample was developed in AZ351 1 : 4 for 12 s, stopping the developing process with H_2O.

Metalization

For metalization, the Leybold e-beam evaporator was used. This evaporator has four water cooled evaporation sources. The system can be used to evaporate very thin and high quality layers. The aperture consists out of a 10 nm titanium adhesion layer and a 120 nm gold layer. For the lift-off, the sample was put into acetone for four hours. Figure 3.7 depicts one sample after the lift off process.

Figure 3.7: Scanning electron microscope picture of the fabricated grating with a gold aperture. The opening is 1.9 × 1.9 mm^2 large.

3.2.3 Doping of graphene

First measurements of a graphene grating did not reveal any plasmon resonance peaks. Due to the position of the Fermi level, transitions are allowed where all photons get absorbed and an excitation of a plasmon is not possible. Doping of the graphene causes a shift of the Fermi level. Hence, some transitions are forbidden and a part of the electrons can be used to excite plasmons. Graphene

can either be p- type (hole) or n-type (electron) doped. Doping with holes shifts the Fermi level beneath the Dirac point, while doping with electrons shifts the Fermi level above the Dirac point. In general, p-doping is achieved by adding atoms with less electrons than carbon and n-doping is achieved using atom with more valence electrons than carbon. Boron or nitric acid, for example, can be used for hole doping and nitrogen can be used as a n-type dopant because it owns more electrons than carbon.

In this work nitric acid was used to achieve a shift of the Fermi level. Graphene can be doped using nitric acid (HNO_3) by vaporizing [2] or putting a sample into liquid nitric acid [42]. Graphitic materials become p-doped when put into nitric acid. The electrons from the graphene are transferred to the nitric acid as given by [42]

$$6HNO_3 + 25C \longrightarrow 25C^+NO_3^- \cdot 4HNO_3 + H_2O, \tag{3.1}$$

causing a shift of the Fermi level under the Dirac point. Thus, transitions beneath $2 \cdot E_F$ are forbidden. The samples were put into 65 % nitric acid for around 7min, rinsed in water and dried with a stream of nitrogen.

3.3 Characterization with Raman spectroscopy

Raman spectroscopy is a powerful tool for the characterization of graphene. Ferrari et. al [27] and Das et. al [43] applied Raman spectroscopy to graphene to measure the number of layers, the doping level, and structural defects. Das et.al showed the dependence of the position and intensity of the G peak on the doping level, as well as the influence on the 2D peak. Figure 3.8 depicts the dependence on the G peak position on the doping (left), as well as the relation between the dependence of the 2D/G ratio (right).

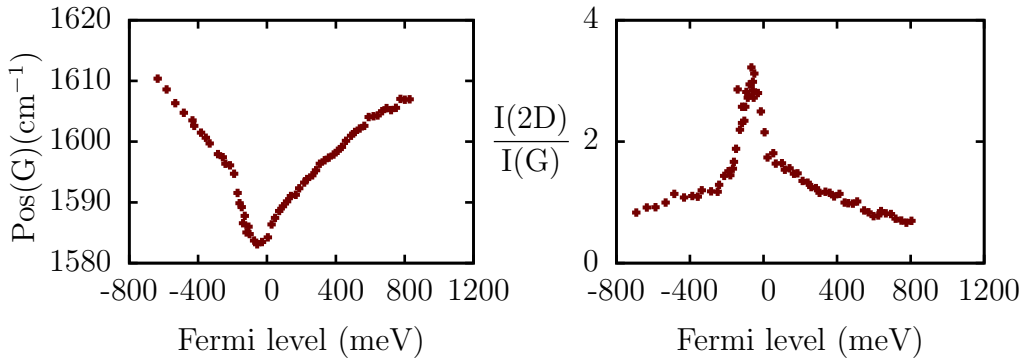

Figure 3.8: Dependence of the G peak position on the Fermi level (left). The right figure depicts the dependence of 2D/G ratio on the Fermi level. The experimental data points are taken from [43].

Figure 3.9 depicts the Raman measurement of a periodically structured graphene grating before and after doping. Beside the characteristic G and 2D band, a third

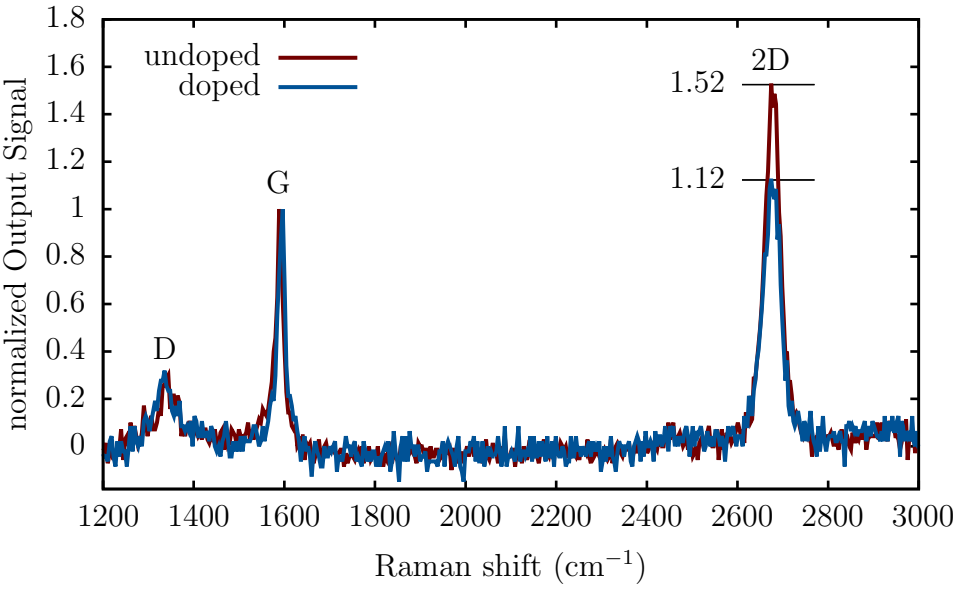

Figure 3.9: Raman spectra of a graphene grating before and after doping with nitric acid. Due to disorder, the D band can be observed in the spectrum. The G band is normalized to one. The shift of the G peak as well as the changed relation between the intensity of the G and 2D peak indicates doping.

band can be observed at around 1350 cm^{-1}. This band is referred to as D band and indicates disorder or defects in graphene. The D band in Figure 3.9 arises from the edges of the graphene bars. A shift of the G band peak and the relation of the intensity between G and 2D peak suggest the presence of doping. Thus Raman spectroscopy can be used to determine the doping level. The G band of both Raman spectra in Figure 3.9 are normalized to one. The relation of the 2D/G is for undoped graphene 1.52 and for doped graphene 1.12, indicating doping. Due to the high dependence of the 2D mode on doping, it is a good indicator for doping. As mentioned before, the position of the G peak also indicates doping. Figure 3.10 illustrates the shift of the G band from figure 3.9. The position of the peaks can be extracted from a Loretzian fit for the undoped sample at 1589.1 cm^{-1} and for the doped sample at 1593.84 cm^{-1}. According to figure 3.8, a shift from $E_\mathrm{F} = -160\,\mathrm{meV}$ to $E_\mathrm{F} = -210\,\mathrm{meV}$ can be extracted. The carrier density can be calculated using

$$p = \int_E \frac{2E}{\pi(\hbar v_\mathrm{F})^2} \left[1 - \frac{1}{\exp\left(\frac{E - E_\mathrm{F}}{k_\mathrm{B}T}\right) + 1}\right] dE. \tag{3.2}$$

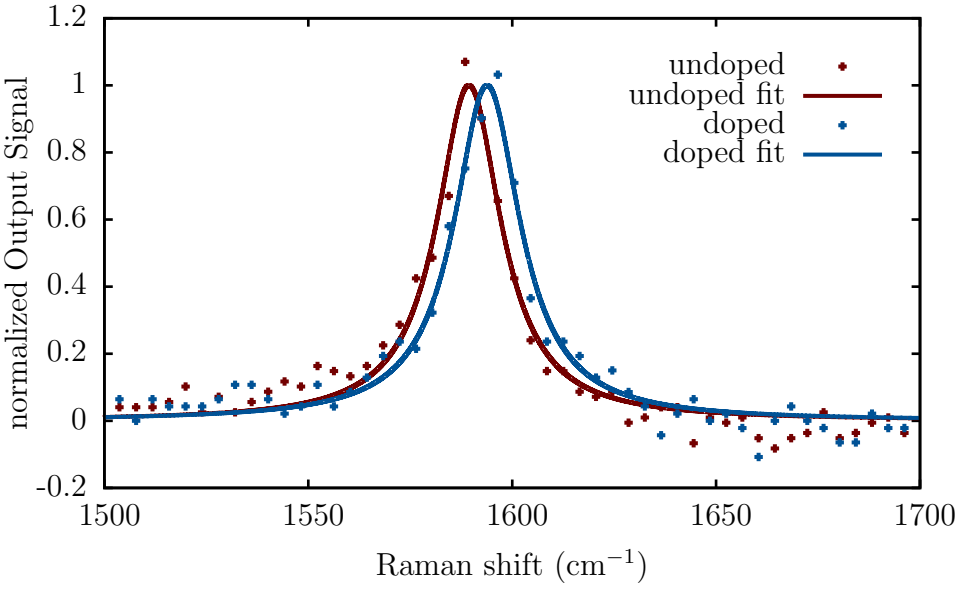

Figure 3.10: Enlargement of the G band from figure 3.9. The G peak shifts from 1589.1 cm^{-1} to 1593.84 cm^{-1} due to doping. The peak position was extracted with a Lorentzian fit.

3.4 Transmittance measurements

The electromagnetic response of the fabricated nanostructures was characterized by transmittance measurements using Fourier spectroscopy. The graphene nanostructures were measured in the mid infrared range. The transmittance of such plasmonic structures depends on the polarization due to their geometric form. As the optical properties of such nanostructures naturally depend on the polarization, the effect of the plasmon on the transmittance or absorption can be described as

$$1 - \frac{T_\perp}{T_\parallel}, \tag{3.3}$$

where $T_\parallel$ denotes light with a polarization parallel to the graphene grating and $T_\perp$ denotes light with a polarization perpendicular to the graphene grating. Due to Pauli blocking of interband transitions the interaction of highly doped graphene with parallel polarized light is insignificant as depicted in chapter 2. The fabricated graphene samples were measured using the Bruker Fourier spectrometer in conjunction with a broadband polarizer. The sample chamber was purged with nitrogen and all measurements were done at room temperature. Figure 3.11 depicts the excitation spectrum of a graphene grating with a period of 250 nm. The inset shows the original data and the constant background indicated with dashed lines. This background stems from a broad and strong absorption of the SiO_2 substrate that appears to be slightly different for s- and p-polarization. This background

was subtracted to get a better illustration of the resonance peaks. The spectrum contains three dominant absorption peaks. The first and second peaks arise from interactions of graphene plasmons with the substrate (SiO_2) phonons. These so called Fuchs Kliever optical surface phonons are well known on polar semiconductor surfaces. Due to long - range Fröhlich coupling these surface optical phonons interact with the graphene layer. The third peak is the surface plasmon polariton excited in the graphene sheet.

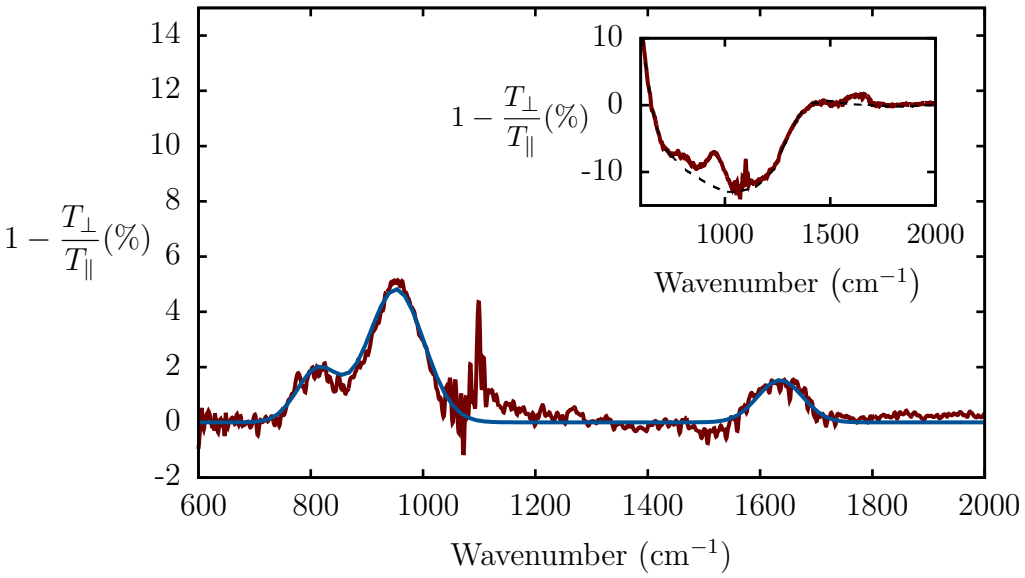

Figure 3.11: Fourier spectrum of a graphene grating with a grating period of 250 nm. The inset shows the original measured data and the background indicated with the dashed line. The background is subtracted from the original data for a better illustration. Three dominant resonance peaks can be observed in the spectrum. The first and second peak indicate the presence of surface polar phonons from the silicon dioxide, which couple with the electrons in graphene. The third peak results from a surface plasmon polariton on the graphene grating. The blue line depicts the fit of the resonance peak to determine the position.

A second graphene grating was fabricated to examine the influence of the grating period on the resonance spectrum due to the dependence of the plasmon frequency on the grating period, as depicted in Ref. [2] as

$$\omega_{\mathrm{spp}} = \sqrt{\frac{\beta E_{\mathrm{F}} e^2}{2\pi\hbar^2 \epsilon_0 \epsilon_{env}}}, \tag{3.4}$$

with $\beta \propto \sqrt{2\pi/d_{\mathrm{p}}}$, where d_{p} denotes the grating period. The second grating was fabricated with a grating period of 440 nm. The grating was fabricated similar to the first one. Figure 3.12 depicts the Fourier spectrum of the second grating.

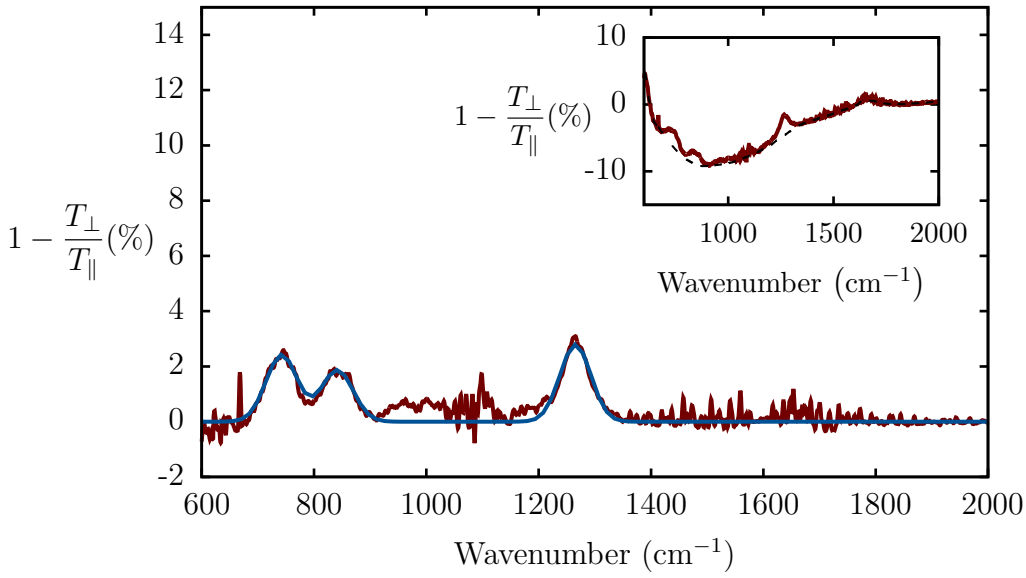

Figure 3.12: Fourier spectra of a graphene ribbon grating with a grating period of 440 nm. The inset depicts the original measured data and a constant background indicated with the black dashed line. For better illustration the background is subtracted from the original data. Three dominant resonance peaks can be monitored. The first and second are due to coupling of surface phonons with the graphene. The third peak is related to the surface plasmon on the graphene grating.

Comparing the resonance spectra of the two different gratings, we make the following observations. Increasing the grating period leads to a red shift of all resonance peaks to lower frequencies. The third peak shifts stronger than the other peaks. Furthermore, the spectral weight of the peaks also depends on the grating period. The spectral weight of the first peak becomes larger when the grating period is increased, while the spectral weight of the second peak becomes smaller. Furthermore the spectral weight of the third peak decreases due to plasmon damping [2].

The three resonance peaks can be described using the random phase approximation (RPA) theory. This theory enables a description of the inverse dielectric function, which represents the ability of the system to dissipate energy via plasmon excitation [2]. It includes interactions with the substrate phonons of silicon dioxide as well as interaction with graphene optical phonon modes. Substrate phonons are due to the optical piezoelectric modes in a polar substrate such as silicon dioxide. The carriers in graphene couple with the electric field of these modes. In the long wavelength range this can be described using the RPA theory via the dielectric function of the substrate. The dielectric function includes direct Coulomb interaction, interaction with surface phonons and optical phonon interac-

tions. The imaginary part of the inverse dielectric function describes the losses due to the mentioned interactions. The plasmon phonon modes can be straight forward calculated, neglecting substrate phonon interactions. The dielectric function for $\omega > \omega_{sp1}$ and $\omega > \omega_{sp2}$ is given as [2]

$$\epsilon_T^{rpa} \approx \epsilon_{env}\left[1 - \frac{\omega_{\mathrm{spp}}^2(\beta)}{(\omega+\imath\delta_e)^2} - \frac{\tilde{\omega}_{sp1}^2}{(\omega+\imath\delta_{sp})^2 - \omega_{sp1}^2 + \tilde{\omega}_{sp1}^2} - \frac{\tilde{\omega}_{sp2}^2}{(\omega+\imath\delta_{sp})^2 - \omega_{sp2}^2 + \tilde{\omega}_{sp2}^2}\right], \tag{3.5}$$

where $\omega_{sp1,2}$ are the surface phonon modes of silicon dioxide. Neglecting single particle damping and surface phonon damping $\delta_e = \delta_{sp} = 0$, the frequencies of the phonon modes can be derived with $\epsilon_T^{rpa} = 0$. The plasma frequency ω_{spp} depending on the wave vector can be calculated from equation 3.4. Including the dependence of the Fermi level as well as the dependence on the environment of graphene with ϵ_{env}. The coupling between the optical piezoelectric modes from the substrate with the graphene is included via

$$\tilde{\omega}_{sp1,2} = \sqrt{\frac{4\pi}{\hbar}\omega_{sp1,2}\mathcal{F}_{1,2}^2}, \tag{3.6}$$

where $\mathcal{F}_{1,2}^2$ denotes the coupling strength of the surface phonon modes. Figure 3.13 illustrates the coupled plasmon phonon modes from equation 3.5 with the plasmon dispersion given in equation 3.4 (red) and the frequency peaks of the two gratings extracted from figure 3.11 (black dots) and figure 3.12 (black dots). The calculations assume doped graphene with a Fermi level $E_{\mathrm{F}} = -600\,\mathrm{meV}$ and an effective permittivity $\epsilon_{env} = 1.5$. The frequency of the first phonon mode is assumed to be at $\omega_{sp1} = 806\,\mathrm{cm}^{-1}$ with a Fröhlich coupling parameter $\mathcal{F}_1^2 = 3.5\,\mathrm{meV}$. The second phonon mode is assumed to be at $\omega_{sp1} = 1168\,\mathrm{cm}^{-1}$ with a coupling strength of $\mathcal{F}_2^2 = 15.2\,\mathrm{meV}$. Surprisingly, $\mathcal{F}_{1,2}^2$ is around $10\times$ larger than in Ref.[2]. Equation 3.5 includes both phonon modes and the interaction with each other. Due to their interaction the bands overlap, and energy dissipation between two bands occur. This can be seen by comparing the resonance spectra of the different gratings. The spectral weight of the first peak is transferred to the second peak.

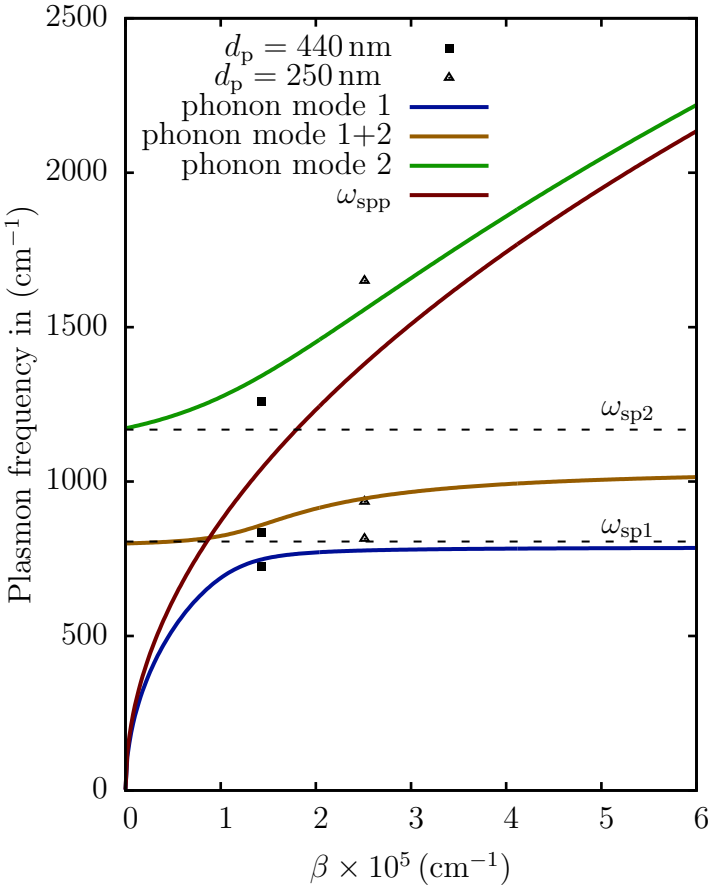

Figure 3.13: Dependence of the plasmon frequency on the wave vector. The red line depicts the classical approach. The resonance peaks for each grating are marked with black dots. The two surface phonon modes are assumed to be at $\omega_{sp1} = 806\,\mathrm{cm}^{-1}$ and $\omega_{sp1} = 1168\,\mathrm{cm}^{-1}$ [2]. The coupling strengths for the various modes are set to $\mathcal{F}_1^2 = 3.5\,\mathrm{meV}$ and $\mathcal{F}_2^2 = 15.2\,\mathrm{meV}$.

Chapter 4

Conclusion and Outlook

In conclusion we have demonstrated the excitation of surface plasmon polaritons in patterned CVD graphene in the mid infrared. Sub-wavelength plasmonic structures were fabricated using electron beam lithography and reactive ion etching. The area of the structured graphene was $2 \times 2\,\mathrm{mm}^2$ surrounded by a gold aperture to improve the signal to noise ratio. Two gratings with grating periods of 250 nm and 440 nm were fabricated. The different grating periods allowed us to determine the influence of the ribbon width on the plasmon frequency. The graphene nanostructures were characterized using Raman spectroscopy to determine structural defects and doping. The transmittance measurements were done with a Fourier spectrometer and a broadband polarizer. Three dominant resonance peaks have been observed. Two resonance peaks arise from the interaction of the graphene plasmon with the surface phonon modes of the silicon substrate while the third peak indicates the surface plasmon polariton in graphene. Due to a change of the grating period, three major trends have been observed. From our measurements we conclude that an increase of the grating period gives rise to a red shift of all frequency peaks. Furthermore, an increase of the grating period results in a change of the spectral weight of the surface phonon modes. This is due to the interaction with the surface phonon mode bands. The third trend which can be observed is the broadening of the third peak when the grating period is decreased. This is related to plasmon damping.

Plasmonic structures allow the confinement of electromagnetic fields beyond the diffraction limit. Thus applications like metamaterials, quantum optics as well as photo-voltaic and biological sensing are possible. Plasmonic structures made out of graphene benefit from a long plasmon life time. A major advantage using graphene as a material for plasmonic structures, is the tunability of the Fermi level by electrical gating or chemical doping as well as the broadband absorption spectrum, enabling new possibilities for light matter interaction.

Bibliography

[1] L. Ju, B. Geng, J. Horng, C. Girit, M. Martin, Z. Hao, H. A. Bechtel, X. Liang, A. Zettl, Y. R. Shen *et al.*, "Graphene plasmonics for tunable terahertz metamaterials," *Nature Nanotechnology*, vol. 6, no. 10, pp. 630–634, 2011.

[2] H. Yan, T. Low, W. Zhu, Y. Wu, M. Freitag, X. Li, F. Guinea, P. Avouris, and F. Xia, "Damping pathways of mid-infrared plasmons in graphene nanostructures," *Nature Photonics*, vol. 7, no. 5, pp. 394–399, 2013.

[3] D. C. b. U. o. C. UC, May 2013. [Online]. Available: http://chemwiki.ucdavis.edu/Organic_Chemistry/Organic_Chemistry_With_a_Biological_Emphasis/Chapter__1%3A_Chapter_1%3A_Introduction_to_organic_structure_and_bonding_I/Section_5%3A_Valence_bond_theory%3A_sp,_sp2,_and_sp3_hybrid_orbitals

[4] A. C. Neto, F. Guinea, N. Peres, K. Novoselov, and A. Geim, "The electronic properties of graphene," *Reviews of Modern Physics*, vol. 81, p. 109, 2009.

[5] P. Avouris, "Graphene: electronic and photonic properties and devices," *Nano Letters*, vol. 10, no. 11, p. 4285, 2010.

[6] D. R. Cooper, B. DAnjou, N. Ghattamaneni, B. Harack, M. Hilke, A. Horth, N. Majlis, M. Massicotte, L. Vandsburger, E. Whiteway *et al.*, "Experimental review of graphene," *ISRN Condensed Matter Physics*, vol. 2012, 2012.

[7] M. I. Katsnelson, "Graphene: carbon in two dimensions," *Materials today*, vol. 10, no. 1, pp. 20–27, 2007.

[8] K. Fai Mak, L. Ju, F. Wang, and T. F. Heinz, "Optical spectroscopy of graphene: From the far infrared to the ultraviolet," *Solid State Communications*, vol. 152, no. 15, pp. 1341–1349, 2012.

[9] K. F. Mak, M. Y. Sfeir, Y. Wu, C. H. Lui, J. A. Misewich, and T. F. Heinz, "Measurement of the optical conductivity of graphene," *Physical Review Letters*, vol. 101, no. 19, p. 196405, 2008.

[10] K. Novoselov, A. Geim, S. Morozov, D. Jiang, Y. Zhang, S. Dubonos, I. Grigorieva, and A. Firsov, "Electric field effect in atomically thin carbon films," *Science*, vol. 306, no. 5696, pp. 666–669, 2004.

[11] X. Li, W. Cai, J. An, S. Kim, J. Nah, D. Yang, R. Piner, A. Velamakanni, I. Jung, E. Tutuc *et al.*, "Large-area synthesis of high-quality and uniform graphene films on copper foils," *Science*, vol. 324, no. 5932, pp. 1312–1314, 2009.

[12] K. V. Emtsev, A. Bostwick, K. Horn, J. Jobst, G. L. Kellogg, L. Ley, J. L. McChesney, T. Ohta, S. A. Reshanov, J. Röhrl *et al.*, "Towards wafer-size graphene layers by atmospheric pressure graphitization of silicon carbide," *Nature Materials*, vol. 8, no. 3, pp. 203–207, 2009.

[13] P. Avouris and C. Dimitrakopoulos, "Graphene: synthesis and applications," *Materials Today*, vol. 15, no. 3, pp. 86–97, 2012.

[14] V. C. Tung, M. J. Allen, Y. Yang, and R. B. Kaner, "High-throughput solution processing of large-scale graphene," *Nature nanotechnology*, vol. 4, no. 1, pp. 25–29, 2008.

[15] A. K. Geim, "Graphene: status and prospects," *Science*, vol. 324, no. 5934, pp. 1530–1534, 2009.

[16] O. L. Congqin Miao, Churan Zheng and D. S. M. E. Ya-Hong Xie, "Chemical vapor deposition of graphene from physics and applications of graphene - experiments," in *Physics and Applications of Graphene - Experiments*. intechopen.com, 2011.

[17] A. Reina, X. Jia, J. Ho, D. Nezich, H. Son, V. Bulovic, M. S. Dresselhaus, and J. Kong, "Large area, few-layer graphene films on arbitrary substrates by chemical vapor deposition," *Nano letters*, vol. 9, no. 1, pp. 30–35, 2008.

[18] H. Ueta, M. Saida, C. Nakai, Y. Yamada, M. Sasaki, and S. Yamamoto, "Highly oriented monolayer graphite formation on Pt (111) by a supersonic methane beam," *Surface science*, vol. 560, no. 1, pp. 183–190, 2004.

[19] J. Coraux, T. N. Plasa, C. Busse, T. Michely *et al.*, "Structure of epitaxial graphene on ir (111)," *New Journal of Physics*, vol. 10, no. 4, p. 043033, 2008.

[20] M. S. Lundstrom, "Graphene: the long and winding road," *Nature Materials*, vol. 10, no. 8, pp. 566–567, 2011.

[21] Y. Zhu, S. Murali, W. Cai, X. Li, J. W. Suk, J. R. Potts, and R. S. Ruoff, "Graphene and graphene oxide: synthesis, properties, and applications," *Advanced materials*, vol. 22, no. 35, pp. 3906–3924, 2010.

[22] F. Bonaccorso, Z. Sun, T. Hasan, and A. Ferrari, "Graphene photonics and optoelectronics," *Nature Photonics*, vol. 4, no. 9, pp. 611–622, 2010.

[23] L. G. De Arco, Y. Zhang, A. Kumar, and C. Zhou, "Synthesis, transfer, and devices of single- and few-layer graphene by chemical vapor deposition," *Nanotechnology, IEEE Transactions on*, vol. 8, no. 2, pp. 135–138, 2009.

[24] S. Bae, H. Kim, Y. Lee, X. Xu, J.-S. Park, Y. Zheng, J. Balakrishnan, T. Lei, H. R. Kim, Y. I. Song *et al.*, "Roll-to-roll production of 30-inch graphene films for transparent electrodes," *Nature nanotechnology*, vol. 5, no. 8, pp. 574–578, 2010.

[25] N. Zhan, M. Olmedo, G. Wang, and J. Liu, "Layer-by-layer synthesis of large-area graphene films by thermal cracker enhanced gas source molecular beam epitaxy," *Carbon*, vol. 49, no. 6, pp. 2046–2052, 2011.

[26] P. Blake, E. Hill, A. C. Neto, K. Novoselov, D. Jiang, R. Yang, T. Booth, and A. Geim, "Making graphene visible," *Applied Physics Letters*, vol. 91, p. 063124, 2007.

[27] A. Ferrari, J. Meyer, V. Scardaci, C. Casiraghi, M. Lazzeri, F. Mauri, S. Piscanec, D. Jiang, K. Novoselov, S. Roth *et al.*, "Raman spectrum of graphene and graphene layers," *Physical Review Letters*, vol. 97, no. 18, p. 187401, 2006.

[28] M. Hesse, H. Meier, and B. Zeeh, *Spektroskopische Methoden in der organischen Chemie*. Georg Thieme Verlag, 2005.

[29] A. Pospischil, "Electrical transport in atomically thin MoS2 layers," Master's thesis, Technical University Vienna, 2012.

[30] H. Yan, F. Xia, W. Zhu, M. Freitag, C. Dimitrakopoulos, A. A. Bol, G. Tulevski, and P. Avouris, "Infrared spectroscopy of wafer-scale graphene," *ACS Nano*, vol. 5, no. 12, pp. 9854–9860, 2011.

[31] S. A. Maier, *Plasmonics: fundamentals and applications*. Springer Science+ Business Media, 2007.

[32] P. B. Johnson and R. Christy, "Optical constants of the noble metals," *Physical Review B*, vol. 6, no. 12, p. 4370, 1972.

[33] G. A. Reider, *Photonik*. Springer DE, 2007.

[34] Q. Bao and K. P. Loh, "Graphene photonics, plasmonics, and broadband optoelectronic devices," *ACS Nano*, vol. 6, no. 5, pp. 3677–3694, 2012.

[35] Y. V. Bludov, A. Ferreira, N. Peres, and M. Vasilevskiy, "A primer on surface plasmon-polaritons in graphene," *arXiv preprint arXiv:1302.2317*, 2013.

[36] M. Jablan, H. Buljan, and M. Soljačić, "Plasmonics in graphene at infrared frequencies," *Physical Review B*, vol. 80, no. 24, p. 245435, 2009.

[37] M. P. I. Max Planck Institute for the science of light, May 2013. [Online]. Available: http://www.mpl.mpg.de/en/institute/technology-development-andservice-units/tdsu-1micro-nanostructuring/lithography/tools.html

[38] N. S. Cornell and T. Facility, May 2013. [Online]. Available: http://www.cnf.cornell.edu/cnf_spietoc.html

[39] P. C. Louisiana Tech University Institute for Micromanufactoring, May 2013. [Online]. Available: http://140.120.11.121/~denda/Upload/paper/%5B11%5DIntroduction%20to%20Electron%20Beam%20Lithography.pdf

[40] H. Jansen, H. Gardeniers, M. de Boer, M. Elwenspoek, and J. Fluitman, "A survey on the reactive ion etching of silicon in microtechnology," *Journal of Micromechanics and Microengineering*, vol. 6, no. 1, p. 14, 1996.

[41] T. W. Zentrum für Mikro-und Nanostrukturen der TU Wien, May 2013. [Online]. Available: http://zmns.tuwien.ac.at

[42] A. Kasry, M. A. Kuroda, G. J. Martyna, G. S. Tulevski, and A. A. Bol, "Chemical doping of large-area stacked graphene films for use as transparent, conducting electrodes," *ACS Nano*, vol. 4, no. 7, pp. 3839–3844, 2010.

[43] A. Das, S. Pisana, B. Chakraborty, S. Piscanec, S. Saha, U. Waghmare, K. Novoselov, H. Krishnamurthy, A. Geim, A. Ferrari *et al.*, "Monitoring dopants by raman scattering in an electrochemically top-gated graphene transistor," *Nature Nanotechnology*, vol. 3, no. 4, pp. 210–215, 2008.